Contact loss in all solid-state Li-ion batteries via deposition of impurities

Sundeep Vema[1,2], James A. Gott[3], Hao Yin[4], Ashley M. Roach[4], Geoff West[3], Norman A. Fleck[4], Vikram S. Deshpande[4, *] and Clare P. Grey[1, 2, *]

[1] Yusuf Hamied Department of Chemistry, University of Cambridge, Lensfield Road, Cambridge, CB2 1EW, United Kingdom
[2] The Faraday Institution, Quad One, Harwell Campus, Didcot, OX11 0RA, United Kingdom
[3] Warwick Manufacturing Group (WMG), University of Warwick, Coventry, CV4 7AL, United Kingdom
[4] Department of Engineering, University of Cambridge, Trumpington Street, Cambridge, CB2 1PZ, United Kingdom

Abstract

Solid-state batteries promise high energy storage with enhanced safety but suffer from contact loss at the lithium (Li) metal anode-solid electrolyte interface as Li is stripped into the ionically conducting solid electrolyte. Our measurements demonstrate that, in cells with garnet electrolytes, an important but overlooked mechanism for contact loss arises from the deposition of insulating impurities from within the Li electrode onto the interface. These impurities form a porous layer, and an imposed stack pressure is required for Li to creep through this layer. Insufficient stack pressure results in empty pores between the impurity particles and these pores resemble inter-connected nano to micro-scale voids. This proposed mechanism is supported by our direct observations of the interface and by our finding that contact loss persists at stack pressures which are sufficiently high to collapse any voids in the Li that are not mechanically supported by the skeleton of impurity particles. Theoretical models developed using the impurity deposition mechanism are in excellent agreement with measurements. This finding has significant implications for improving the design of all solid-state batteries including the development of anode-free cells for which impurities within the electrode are expected to be substantially reduced.

Introduction

Lithium-ion batteries with lithium (Li) metal anodes can deliver higher specific energy densities[1]. However, with liquid electrolytes, non-uniform deposition of Li ions onto the Li metal electrode leads to the formation of mossy structures and dendrites that subsequently grow through the porous separator and short-circuit the battery. It was hoped that the high shear modulus of solid ceramic electrolytes would mechanically suppress dendrite formation[2]. Furthermore, ceramic electrolytes do not contain volatile and flammable organic components and thereby possess high thermal stability and enhanced safety[3]. Experimental observations have, however, revealed that solid-state batteries also fail by short-circuiting due to the penetration of Li filaments through the ceramic electrolyte. This failure mode operates at currents exceeding the so-called "critical current density"[4].

Bruce and co-workers[5] identified two distinct critical current densities: the critical current for stripping (CCS), and the critical current for plating (CCP). They observed that Li filaments initiate and grow in Argyrodite ($\mathrm{Li_6PS_5Cl}$) electrolytes when Li metal is plated onto the electrode at a current that exceeds the CCP. Conversely, stripping the Li metal electrode leads to "loss of contact" between the electrode and electrolyte when the CCS is exceeded. They reported a lower value of CCS than that of CCP. Subsequent studies[6–8] reported contact loss at Li/LLZO (Li stuffed or doped garnet, $\mathrm{Li_7La_3Zr_2O_{12}}$) interfaces. These studies observed that the critical stripping capacity at which contact loss occurs is dependent on electrode thickness and cell current[9].

Contact loss is often inferred (i.e., measured) by an increase in the cell voltage, which is then associated with an increase in the resistance of the stripping interface. While this voltage increase has been reported by numerous studies[5,6], the mechanisms of this contact loss remain unclear, and it is commonly attributed to void growth at the interface[6–8,10,11] (Fig. 1a). However, direct observations of interfacial voids in Li cells are more limited: for example, Krauskopf et al.[7] and Lu et al.[12] reported void observations but these observations involved either peeling of the electrode from the electrolyte or sectioning of the cell under conditions that could have caused damage. While tomographic observations of voids in Sodium (Na) electrodes and Na/Na-β'' electrolytes[13] and in Li electrodes with Argyrodite electrolytes[14] have been reported, the use of interactive thresholding to identify voids introduces a level of uncertainty given the relatively low X-ray absorbance of Na as well as Li and the consequent poor contrast between the metal and other components such as voids and impurities such as metal oxides. Moreover, even if void formation is the mechanism of contact loss, the process by which these voids form and grow remains unclear. The literature has focussed on two mechanisms: (I) creep deformation and vacancy diffusion within the metal electrode[5,7] and (ii) the electrochemical kinetics at the electrode/electrolyte interface[9,15–19] leading to focussing of flux around imperfections on the interface. While some earlier models[7] (i) suggest that vacancy diffusion plays a dominant role, using the Onsager formalism, Shishvan et al.[20] showed that there exists no driving force to drive kinetic processes associated with vacancy diffusion and coalescence. This conclusion is consistent with the established literature[21–23] on electromigration which concludes that void nucleation based on a vacancy condensation mechanism requires an unrealistically high concentration of vacancies that is difficult to justify from a thermodynamic point of view, unless more complex interfaces are considered. Mechanism (ii) assumes that void growth from pre-existing micro-voids/impurities occurs by power law creep of the Li[16,18]: modifications to standard Butler-Volmer kinetics[16,19] are needed to predict sufficient flux focussing to drive void growth. Even if these modified kinetics are appropriate, voids would collapse rather than grow under the typical stack pressures at which most experiments are conducted. For example, most experiments[5,24,25] are carried out at stack pressures above 5 MPa:

given that the creep strength of Li is ~ 1 MPa it would be surprising that voids can grow and cause contact loss. In fact, recent observations and measurements by Roach et al.[26] confirm the high rate at which voids collapse in Li for stack pressures exceeding 1 MPa. Nevertheless, contact loss as measured by the increase in cell voltage has been extensively observed.

A combination of measurements, observations of the electrode/electrolyte interface, and theoretical modelling has led us to re-examine the hypothesis that contact loss occurs solely via void growth in the Li at the electrode/electrolyte stripping interface. Our analyses show that contact loss is associated with the deposition of insulating impurities from within the Li electrode on the stripping interface as Li is stripped into the electrolyte (here LLZO). For contact to be maintained, the imposed stack pressure needs to drive the Li via creep through the gaps between these impurity particles. With insufficient stack pressures, the rate at which Li ions are transported into the LLZO electrolyte exceeds the rate at which Li is replenished by the creep of Li through the gaps between the impurity particles. This situation results in the formation of pores within the impurity layer, and these pores resemble inter-connected micro to nano-scale voids.

Our study uses the Li/LLZO all solid-state battery system. Al-LLZO powder was hot-pressed to achieve pellets of porosity less than 1%. Li-LLZO-Li cells without any interlayers were then fabricated using these pellets (*Methods*). For each cell, potentiostatic electrochemical impedance spectroscopy (PEIS) was performed to estimate the Li-LLZO interfacial resistance (*Methods*). Only samples with interfacial resistances Z below $20\ \Omega\text{cm}^2$ were used in this study. Galvanostatic measurements (Fig. 1b) were conducted on these low interface resistance cells using an imposed stack pressure of up to 15 MPa. The focus here is to investigate failure mechanisms on the stripping interface (i.e., contact loss). Thus, to avoid failure by the initiation of dendrites on the plating interface, the symmetry of the cell was broken such that the electrode area on the plating interface was 2.25 times that of the stripping interface (Fig. 1b). This arrangement leads to a lower current density on the plating interface, thereby inhibiting dendrite growth in all our measurements.

Results

Contact loss is accompanied by the formation of a layer of impurities on the interface

Measurements were conducted with a fixed imposed cell current and stack pressures p in the range $5\text{ MPa} \leq p \leq 15\text{ MPa}$. First consider the case when the interface resistance $Z \approx 9\ \Omega\text{cm}^2$. The temporal variation of the cell voltage V_{cell} for an imposed stripping electrode current density $i_s = 1\text{ mAcm}^{-2}$ (Fig. 1c) shows a strong sensitivity to stack pressure (i_s is defined as the ratio of the imposed current to the area of the stripping interface). With contact loss defined as the time t_f when $V_{\text{cell}} = 5\text{ V}$, we observe that the critical capacity $C_{\text{cr}} \equiv i_s t_f$ and time t_f at cell failure, increases with increasing p. Note that the steeply rising voltage-versus-capacity curve at $V_{\text{cell}} = 5\text{ V}$ implies that C_{cr} is insensitive to the choice of voltage for $V_{\text{cell}} \geq 5\text{ V}$. Three-electrode measurements confirmed that, in line with previous studies[6], the increase in cell voltage was due to an increase in the stripping interface resistance while the plating interface resistance remains unchanged (Fig. S1).

The increase in cell voltage is commonly attributed to contact loss associated with void growth in the Li at the stripping interface (Fig. 1a). To determine whether this is the correct explanation *in our system*, we conducted high resolution, cryo-plasma focussed ion beam (PFIB) sectioning combined with scanning electron microscope (SEM) observations of both the pristine interface (prior to galvanostatic testing) and the stripped interface. The PFIB operation was conducted using very low milling currents to achieve minimal disturbance of the interface (*Methods*).

First, consider the pristine interface where only a PEIS measurement was conducted on an as-manufactured cell to determine the interface resistance; currents of less than $5\ \mu\mathrm{Acm}^{-2}$ were used in the PEIS measurements. An image of the cross-section through the cell ($Z \approx 9\ \Omega\mathrm{cm}^2$) is included in Fig. 2a at two levels of magnification. A sparse scattering of impurity particles on the interface is observed on an otherwise well-bonded interface. The impurity particles are relatively large ($\sim 0.2\ \mu\mathrm{m}$) and energy dispersive X-ray spectroscopy (EDS) maps of the interface show a relatively clean interface with no clear traces of impurity elements. Second, consider the experiment in Fig. 1c with $p = 10$ MPa. This cell had a similar interface resistance of $Z \approx 9\ \Omega\mathrm{cm}^2$ prior to stripping and thus allows for a fair comparison with the pristine interface in Fig. 2a. Representative images of this stripped interface after stripping with $i_s = 1\ \mathrm{mAcm}^{-2}$ for ~ 6 hrs (at which point the cell voltage had risen to 5 V) are included in Fig. 2b at two levels of magnification. This high cell voltage suggests near complete loss of contact at the stripping interface. However, voids within pristine Li (akin to the sketch in Fig. 1a) are clearly not observed (at least three different locations were imaged in 3 different cells). Instead, there is a change in the structure of the interface (Fig. 2b) with impurities now clearly visible on the interface and voids present within and around this impurity layer.

EDS maps (Fig. 2b) show the presence of oxygen on the electrode (Li) side of the interface. By contrast, the pristine interface is much cleaner (Fig. 2a), with a clear boundary between the oxygen-containing LLZO electrolyte and the Li metal, suggesting that the deposits in Fig. 2b are Li-based oxides. No indication of La, Zr and Al can be seen at the interface (Fig. S2) suggesting that the observed impurities observed are neither due to redeposition during milling, nor are related to migration of ions such as Al^{3+}, out of the LLZO. Moreover, we refer to the impurities as deposits as they are observed even at much lower cell voltages where decomposition of the LLZO is not expected (see Fig. S3 for equivalent micrographs of the interface taken after the cell voltage had reached 2V with stripping currents $i_s = 1\ \mathrm{mAcm}^{-2}$ and $0.3\ \mathrm{mAcm}^{-2}$). We conclude that the voids in Fig. 2b are not voids in pristine Li as hypothesised in Fig. 1a but rather empty pores within the impurity layer: the 10 MPa stack pressure is insufficient to drive Li into these pores by creep. The lack of voids in pristine Li in our observations appears to contradict some previously reported PFIB-SEM observations[12,27,28]. One hypothesis to rationalise this apparent discrepancy is provided by recalling that we have observed the presence of impurities that are weakly bonded to the interface (Fig. 2b). This suggests that the large milling currents (on the order of 2 μA) used in previous studies[12,28] may disturb (and dislodge) impurities during sectioning of the cell by milling likely giving the impression of the presence of voids. To test this hypothesis, we milled a portion of the stripped interface (cell with $p = 10$ MPa in Fig. 1c) using currents of 4 μA and $0.4\ \mu\mathrm{A}$. An SEM image of this interface (Fig. 2c) clearly shows the presence of impurity patches on the portion of the interface milled using a $0.4\ \mu\mathrm{A}$ milling current. On the other hand, the $4\ \mu\mathrm{A}$ milling current disturbs impurities thereby generating cavities between the Li electrode and the LLZO electrode in the sectioned cells. This gives an appearance of voids in pristine Li akin to Fig. 1a. Thus, our observations are consistent with those in the literature, except that our use of careful low milling currents allows for a more accurate determination of the structure of our stripped interfaces.

Contact loss persists in the presence of large stack pressures

Our observations suggest that contact loss may not be due to growth of voids in pristine Li [6,7,9] but rather contact loss in our system occurs by a combination of the formation of an insulating impurity layer and empty pores within this layer. Theoretical calculations, based on a range of mechanisms[19,20] provide additional evidence that void growth in pristine Li should not occur at the stripping interface. This is even more true under a stack pressure of 10 MPa as voids in pristine Li with a creep strength of ~ 1 MPa[29–32] would be expected to rapidly collapse. Measurements[26] have confirmed the collapse of such voids under stack pressures in the range 0.05 – 20 MPa. To appreciate the time scales over which these voids collapse under stack pressure consider a theoretical model involving a hemispherical void of radius a_v at the interface between a large Li electrode and a rigid electrolyte (Fig. 3a and Supplementary Section S1). The electrode is subjected to a stack pressure p and we only consider mechanical loading such that there is no flux of Li ions into the electrolyte. Write V as the void volume at time t after the application of the pressure and V_0 as the initial void volume. Predictions of the temporal evolution of the normalised void volume V/V_0, are included in Fig. 3b (also see Fig. S4 for the predicted spatio-temporal evolution of the void). Calculations are shown assuming that the Li can either freely slip on the interface (no friction) or that it sticks to the interface and for applied stack pressures in the range 5 MPa $\leq p \leq$ 30 MPa. (Note that the normalisation V/V_0 implies that these predictions are independent of a_v). These calculations show that irrespective of the assumed interface boundary condition, the voids collapse after ~100 s and 1s for $p = 5$ MPa and $p = 10$ MPa, respectively (and on the milli-second timescale at higher pressures). These conclusions are further supported by our direct observations which show that voids collapse in ~1 min at stack pressures as low as 1.4 MPa (Fig. S5).

By contrast, contact loss, as measured via the sharp and sudden increase in voltage occurs typically over 30 mins (see upper x-axis scale in Fig. 1c) thus it is unclear why contact loss would occur over such a long timescale when voids collapse in seconds under the imposed stack pressures. The sharp rise in voltage results requires loss of contact that covers almost the whole electrode/electrolyte interface and the sudden generation of a single void by the mechanism of Fig. 1a cannot be responsible for this phenomenon. The high-volume fraction of voids over the electrode/electrolyte interface that resulted in the voltage increase over a timescale of ~ 30 mins would collapse by creep under the imposed stack pressures. Our calculations (Fig. S6) show that artificially increasing the strength of Li to account for possible increases in Li strength at smaller length scales[32] does not change the overall conclusion that, at the stack pressures of 10 MPa and above, voids collapse over a timescale much less than the timescale over which voltage rises are observed.

To improve our understanding, we conducted a series of experiments to quantify the interplay between interface resistance Z, stack pressure p and stripping current density i_s on contact loss. These measurements are summarised in Figs. 3c and 3d in terms of the measured critical capacity C_cr (defined again as the point when the cell voltage rises to 5V). In Fig. 3c we show the dependence of C_cr on the interface resistance Z for three values of the applied stack pressure p and $i_s = 1\ \mathrm{mAcm}^{-2}$. For a given Z, the critical capacity increases with increasing p and for a given p, the capacity decreases with increasing Z but plateaus out at high values of Z. While p has a large effect on C_cr we observed that i_s has only a relatively minor influence. This is illustrated in Fig. 3d where we include experimental measurements of C_cr as a function of Z for an applied $p = 10\ \mathrm{MPa}$ and currents in the range $0.3\ \mathrm{mAcm}^{-2} \leq i_s \leq 1.0\ \mathrm{mAcm}^{-2}$. For example, with $Z \approx 13\ \Omega\mathrm{cm}^2$, C_cr increases slightly from $\sim 4.5\ \mathrm{mAhcm}^{-2}$ to $\sim 6\ \mathrm{mAhcm}^{-2}$ when i_s is decreased from $1.0\ \mathrm{mAcm}^{-2}$ to $0.3\ \mathrm{mAcm}^{-2}$. This difference in C_cr is within the variability in the measurements. The results in Figs. 3c and 3d suggest complex coupling between Z, p (and to a lesser extent i_s), but in all cases the failure times t_f are on the order of hours. In contrast, voids in pristine Li are expected to collapse in < 1 min under these imposed stack pressures (Fig. 3b). This, combined with the fact that we did not observe voids in pristine

Li, but only empty pores and voids associated with the impurity layer, drives us to develop an alternate view of the observed contact loss.

Impurity deposition driven contact loss

The images in Fig. 2 support an alternative mechanism in the form of a layer of impurities on the stripped interface (Fig. 2b) that were absent prior to stripping (Fig. 2a). Given that these impurities are weakly bonded to the interface (and get disturbed when the cell is sectioned with high milling currents), we hypothesise that these impurities exist as solutes within the electrode Given the very high purity of the Li metal (~99.9% Li was used in this study) it is difficult to detect impurity particles within the electrode. Nevertheless, our SEM images (Fig. S7) show some evidence of the existence of such particles that are widely spaced, consistent with the high purity of the Li foil used in this study. These impurities within the electrode advect with the Li as it is stripped (i.e., migrate with the thinning Li electrode as sketched in Fig. 4a) and contribute to contact loss via the mechanism sketched in Fig. 4. These impurities cannot, however, pass through the electrolyte and hence accumulate on the electrode/electrolyte interface. Continued stripping increases the density of these solutes on the interface with the deposits existing as a single layer in places and multiple layers in other locations (Fig. 4a). These solutes are insulating and consequently their presence on the interface reduces the effective area for Li^+ flux across the interface and increases the effective interface resistance, as proposed by Agier et al.[17]. We emphasize that this is a potent mechanism for blocking of the interface with even a sparse impurity concentration in the bulk Li resulting in a high impurity concentration on the two-dimensional (2D) interface after only a few microns of stripping. For example, consider a Li foil with $f = 0.1\%$ volume fraction of impurities of size $a = 50$ nm. Stripping $H = 5$ µm of Li will result in impurities spaced a distance $\ell \approx 0.18$ µm on the interface (Supplementary S2; Eq. S19). These insulating impurities reduce the effective interface area and could potentially block the flux of Li ions across the interface.

To illustrate the effect of this reduction in the effective surface area within a theoretical framework, let f denote the volume fraction of spherical solutes of radius a within the Li electrode. After stripping for a time t with an areal current i_s, a height $H_S = i_s t \Omega_{\mathrm{Li}}/F$ of Li has been stripped from the electrode (F the Faraday constant, Ω_{Li} the molar volume of Li). All solutes within the stripped portion H_S of the electrode remain on the interface. Assuming that these solutes are uniformly distributed as a monolayer on the interface, their spacing 2ℓ after a stripping time t is

$$\ell \approx \ell_t = \sqrt{\frac{4Fa^3}{3f i_s t \Omega_{\mathrm{Li}}}}. \tag{1}$$

An area fraction $\sim(a/\ell)^2$ of the interface blocks the flux of Li^+ across the interface and the effective resistance of interface rises to $Z_{\mathrm{eff}} = Z/[1-(a/\ell)^2]$ where Z is the resistance prior to stripping. Assuming one-dimensional flux, the evolution of cell voltage with capacity $C = i_s t$ for a symmetric cell (and assuming the plating interface remains unaffected) is given by

$$V_{\mathrm{cell}} = i_s \left[Z \left\{ \frac{1}{\left(1 - \frac{3fC\Omega_{\mathrm{Li}}}{4Fa}\right)} + 1 \right\} + \frac{L_E}{\kappa} \right], \tag{2}$$

where κ and L_E are the conductivity and thickness of the electrolyte, respectively. With $Z = 9\ \Omega\mathrm{cm}^2$, $L_E = 1$ mm and $\kappa = 0.47\ \mathrm{mS\ cm}^{-1}$ (the cell parameters for Fig. 1c), the predicted evolution of cell voltage is included in Fig. 1c for the choice $f = 0.1\%$ (the Li foil used in the experiments is ~99.9% pure) and a in the range $25\ \mathrm{nm} \le a \le 75\ \mathrm{nm}$. This simple solute deposition model, based on the reduction of the effective interface area due to deposition of insulating particles, broadly predicts the correct critical capacity using a reasonable range of impurity particle sizes. However, this model, which assumes that the voltage increase is solely due to the reduction in the effective area, predicts no dependence of C_{cr} on stack pressure. This is contrary to the strong experimentally observed pressure dependence wherein C_{cr} increases with increasing pressure (Figs. 1c and 3c).

Our observations of a strong stack pressure dependence of C_{cr} drove us to modify the above hypothesis. We now assume that the deposited solutes form a porous layer on the interface and Li needs to flow through this porous layer to reach the interface and then conduct through the electrolyte. Consistent with our observations (Fig. 2b) the layer is approximately 1 particle thick, and the Li will creep through the gaps between the particles to reach the interface. The Li within the electrode (including the Li within the porous interface) is percolated and thus the only force to drive the Li through this layer to the interface is the imposed stack pressure. Continued stripping can occur when the rate at which the stack pressure driven Li creep rate equals the rate at which the Li is stripped at the interface (Fig. 4b). For a given stack pressure, there is a maximum creep rate of the Li through the gaps and if the stripping rate exceeds this creep rate: the Li at the interface is stripped and cannot be replenished from within the electrode. This results in the formation of pores or micro/nano-scale voids as shown in Fig. 4c, although the good adhesion between the impurity particles and Li implies that the impurity particles remain coated with a thin Li layer that provides electron pathways to the interface (zoom in of Fig. 4c). The empty pores/voids in Fig. 4c fundamentally differ from the voids in pristine Li: the mechanical skeleton of the impurity particles sustains the imposed stack pressure and prevents their collapse. These voids or empty pores cannot collapse under imposed stack pressure but can get refilled when sufficient stack pressure forces the Li into them via creep.

We develop a significantly simplified model (Fig. 5a) for this phenomenon assuming a single layer of spherical particles of radius a uniformly dispersed on the interface with a centre-centre spacing 2ℓ (also see Supplementary S2.2 and Fig. S8 for an analysis of a thick layer of impurity particles that confirms that the single layer approximation is more appropriate). To determine the critical capacity C_{cr} at which Li can no longer be stripped, we calculate the critical value of the spacing $\ell = \ell_{\text{cr}}$ below which the stack pressure cannot force the Li through the gaps between the particles. This gives an implicit relation for the dependence of C_{cr} on p and i_s as (Supplementary S2.3):

$$\left(\frac{4Fa}{3C_{\text{cr}}\Omega_{\text{Li}}f}\right)^{1/2} = \frac{1}{\sqrt{3}}\,(n+3)^{\frac{1}{n+1}}\left(\frac{4\sigma_0}{p}\right)^{\frac{n}{n+1}}\left[\frac{i_s\Omega_{\text{Li}}}{Fa\dot{\varepsilon}_0}\frac{1}{1-\left(\frac{3C_{\text{cr}}\Omega_{\text{Li}}f}{4Fa}\right)}\right]^{\frac{1}{n+1}} + 1, \qquad (3)$$

where $(\sigma_0, \dot{\varepsilon}_0, n)$ are the power law creep constants [29,31] of Li, such that the flow strength is $\sigma_0 = 1$ MPa, the reference strain rate is $\dot{\varepsilon}_0 = 0.01\ \text{s}^{-1}$ and the power law creep exponent is $n = 6.6$ (Supplementary S2.2). To make direct comparisons with the experimental observations we also need to account for the fact that the pristine interfaces (i.e. interfaces prior to stripping) have a range of resistances, Z. We use the observation (Fig. 2a) that the pristine interface too has a small area fraction of impurity particles (which could, for example, be residual surface oxides, hydroxides and carbonates (and other residual impurity phases) that are not removed during thermal treatment[33]). Assuming that insulating spherical particles of radius a_0 are uniformly dispersed a distance $2\ell_0$ apart on the pristine interface, the effective conducting area of the interface is reduced by a factor $[1-(a_0/\ell_0)^2]$ and the resistance Z of the pristine interface is related to the resistance Z_0 of the interface in the absence of particles via $Z = Z_0/[1-(a_0/\ell_0)^2]$. The model (3) is then modified to account for the initial partial coverage of impurity particles (Supplementary S2.3) and can be used to predict the capacity C_{cr} at which flow of Li across the interface is blocked.

Using reasonable estimates for the key parameters, viz. $Z_0 = 1\ \Omega\mathrm{cm}^2$ (the lowest value of Z we measured across 50 cells manufactured in this study), particles of sizes $a_0 = 200$ nm and $a = 130$ nm, and $f = 0.1\%$ we include predictions in Fig. 3c of the dependence of C_{cr} on Z for three choices of the stack pressure. Excellent agreement (to within the scatter of the data) is observed indicating that the model captures the dependence of the critical capacity on stack pressure and interface resistance. The predicted dependence of C_{cr} on current is included in Fig. 3d by giving predictions using the same parameters but two extreme currents, $i_s = 0.3\ \mathrm{mAcm}^{-2}$ and $1.0\ \mathrm{mAcm}^{-2}$, with a stack pressure of $p = 10$ MPa. Again, the predictions capture the measurements to high accuracy including the relatively low dependence of C_{cr} on i_s. The observation that the dependence of C_{cr} on i_s is weak (over the range $0.3\ \mathrm{mAcm}^{-2} \leq i_s \leq 1.0\ \mathrm{mAcm}^{-2}$) but strong on p (over the range $5\ \mathrm{MPa} \leq p \leq 15\ \mathrm{MPa}$) is rationalised via the model as an outcome of the high value of the creep exponent n of Li. We note in passing that void growth by flux focussing[7,12,34] is expected to be amplified with increasing i_s while our measurements suggest a weak dependence of C_{cr} on i_s as captured by the impurity deposition model. The good agreement between our model and experiment allows us to conclude that contact loss is associated with the formation of a layer of insulating solutes that are deposited on the interface as the Li is stripped. Importantly, contact loss occurs when the rate at which Li creeps in the gaps between the particles under the imposed stack pressure cannot keep up with the rate at which Li is stripped at the interface resulting in the formation of empty gaps/pores between the particles that resemble voids. We emphasise that the predictions in Figs. 3c and 3d, which agree with measurements for a range of pressures and stripping currents, are for a given Li source which in the context of our model implies a given set of parameters (a_0, a, f, Z_0). Changing the Li source is likely to change at least (a_0, a, f) and consequently our predictions. The sensitivity of the predicted critical capacity to the choice these parameters related to the Li source are exemplified in additional calculations presented in Fig. S9, and we discuss this further below.

The simplifying assumption of a uniform distribution of impurity particles on the interface provides a reasonably accurate prediction of C_{cr} but clearly this is not how impurity deposition occurs. Impurity deposition is expected to be more non-uniform as sketched in Fig. 4a. While the assumption of a spatially uniform distribution of impurity particles of the interface suffices for predicting the capacity C_{cr}, it has some critical limitations that can be appreciated as follows. First consider the uniform deposition assumption. The evolution of the impurity spacing distributions is sketched in Fig. 5a where we see that the probability density of the particle spacing is a dirac delta function $p(\ell) = \delta(\ell - \ell_t)$ with ℓ_t given by (1) and decreasing with time. Then for $\ell_t > \ell_{\mathrm{cr}}$ the Li reaches the electrode/electrolyte interface under the action of the imposed stack pressure, and the cell voltage only rises due to the reduction in the effective surface area of the interface due to the presence of the insulating impurity particles. Predictions of the voltage versus time curves using this model (Supplementary S2.3 and Fig. S10) show that unlike the observations (Fig. 1c), the model predicts a minimal rise in the cell voltage with sudden loss of contact at $C = C_{\mathrm{cr}}$. We argue that the more gradual attainment of the critical state of loss of contact observed in Fig. 1c is related to the non-uniform deposition of impurities. We proceed to clarify this and the role of the two driving forces, viz. the imposed stack pressure and cell voltage in the context of this non-uniform deposition (also see discussion in Supplementary S2.3).

Consider non-uniform deposition of the particles as shown in Fig. 5b with the corresponding temporal evolution of the probability density $p(\ell)$. While clearly the mean spacing decreases with increasing time, the formation of patches of deposited impurities implies that the distribution also becomes more disperse with a higher standard deviation. The consequence of this is seen in Fig. 5b: with increasing time as the distribution becomes more disperse, the cumulative probability of spacings less than ℓ_{cr} increases. These regions of the interface no longer play any role in the stripping and stripping is restricted to regions of the interface with $\ell > \ell_{\mathrm{cr}}$. The inactive and active regions of the interface are shown schematically in Fig. 5b. The imposed voltage controls the Li-ion flux across the active parts of the interface as set by the usual Butler-Volmer kinetics (the stack pressure has a negligible influence on these kinetics as $p\Omega_{\mathrm{Li}}/F \approx 2$ mV $\ll V_{\mathrm{cell}}$ for $p = 15$ MPa). As the active area of the interface decreases the cell voltage increases to maintain the constant cell current. This gives rise to the more gradual increase in cell voltage immediately prior to attainment of the critical capacity observed in Fig. 1c. This is not predicted when uniform deposition is assumed.

Can contact loss recover by void closure?

Our mechanism of contact loss appeals to the existence of voids or empty pores within the deposited layer of impurity particles. These voids are mechanically supported by the skeleton of impurity particles and under stack pressure will close at a slower rate than voids in pristine Li as the Li needs to creep through the micro-gaps between the impurity particles. The time scale for void closure in the impurity layer and in pristine Li differ significantly. For example, voids in pristine Li close within approximately 1 s under a 10 MPa stack pressure (Fig. 3b) while our calculations (Supplementary S2.3 and Fig. S11) suggest that it will take Li ~1 hr to flow through an impurity layer on the interface under a 10 MPa stack pressure if impurities of radius $a = 130$ nm are spaced at $2\ell \sim 310$ nm (this spacing is approximately the spacing of the particles when stripping is blocked at $i_s = 0.6\ \mathrm{mAcm^{-2}}$). This difference in timescales allows us to design strip-rest experiments to differentiate between these two mechanisms of void formation at the interface.

We conducted strip-rest cycles with a period of two hours: strip at a current density $i_s = 0.6\ \mathrm{mAcm^{-2}}$ for 1 hour followed by 1 hour of rest with no imposed current but a constant stack pressure $p = 10$ MPa maintained during both stripping and rest. Measurements of the cell voltage V_{cell} versus time for ~30 hrs are shown in Fig. 6a. There are two important observations. Overall, the voltage during stripping rises gradually over time consistent with increasing loss of contact (also see Fig. 1c). The voltage-time curve during each stripping phase shows two distinct regimes: (i) a sharp rise in voltage and (ii) a subsequent more gradual rise. At the start of each stripping period (after rest) the voltage has nearly recovered back to the value at time $t = 0$ but then rises rapidly to the voltage at which the second slower rise phase had ended in the previous stripping cycle once the current is reapplied (see zoom-in in Fig. 6a). These observations help us differentiate between the two mechanisms of void formation.

First consider the mechanism of void growth in pristine Li. Recall that voids under a pressure of 10 MPa collapse in approximately 1 s (Fig. 3b). Consequently, we would expect that such voids, if they formed under stripping, would collapse during the 1 hr rest period and erase all memory of the loading history with the resistance (and cell voltage) during a subsequent stripping cycle having a temporal response akin to the first cycle at $t = 0$. This is clearly not the case with the measurements (see inset of Fig. 6a) showing a rapid rise in cell voltage to its value at the end of the previous stripping cycle. Both the timescale of the recovery and the fact that the cell maintains memory of the loading history suggest that void growth in (nominally) pristine Li is not an important contributor to contact loss. Next consider the mechanics of the formation of voids or empty pores in the deposited impurity particle layer. During the rest period, Li slowly creeps through the pores of the impurity layer under the imposed stack pressure and re-establishes contact with the interface (over ~ 1hr in line with the calculations in Fig. S11). This implies that interface resistance (and cell voltage) recovers after the rest period. However, upon recommencement of stripping, the relatively small Li content within the pores of the impurity layer is again very quickly depleted and not replenished sufficiently quickly to keep up with the imposed stripping current. Therefore, the interface resistance (and cell voltage) rises quickly back to the value measured at the end of the previous stripping cycle. This memory effect is also consistent with impurity deposition as the rest period does not disturb the deposited impurities.

Recall that our three electrode measurements (Fig. S1) revealed that the changes in cell voltage during galvanostatic loading are solely attributed to the increase in effective resistance of the stripping interface. Thus, additional insights from the temporal evolution of the total resistance of the cell can be used to provide further evidence that contact loss is associated with impurity deposition. We consider two measurements of cell resistance: (i) the cell resistance during stripping with a cell current I given by $R \equiv V_{\text{cell}}/I$, where V_{cell} is the cell voltage (Fig. 6a) and (ii) PEIS measurements (with effectively zero current) during the rest period (*Methods*). It is worth emphasizing that the changes in resistances inferred here have multiple contributions that include reduction in the active area of the interface, contact loss due to void formation and constriction resistance[35,36] due to impurities on the interface. Our measurements do not differentiate between these contributions and are therefore effective resistances. There are two key observations from the measurements in Fig. 6b: (i) a finite resistance drop ΔR exists between the resistance at the end of stripping period and the start of the ensuing rest period and (ii) a gradual subsequent drop, that is recovery, in resistance is seen over the rest period.

To rationalise the resistance drop ΔR, recall that impurity particle patches exist over the interface with a range of particle spacings (Fig. 5b). The portion of the interface where the spacing is small will not permit the flow of Li across the interface under the imposed stack pressure whereas other parts of the interface where impurity particle spacings are larger will admit Li flow. The critical particle spacing ℓ_{cr} required to block the flow is dependent on the imposed current such that ℓ_{cr} is larger at a higher current i_s (Equation S18 in Supplementary S2.3). Thus, it is expected that a larger fraction of the interface becomes inactive at higher currents resulting in a higher effective interface resistance. The stripping resistance $R \equiv V_{\text{cell}}/I$ in Fig. 6b was measured at a unidirectional current density of $i_s = 0.6 \text{ mAcm}^{-2}$ while the cyclic PEIS measurements were conducted with significantly lowers currents ($< 5 \text{ μAcm}^{-2}$). The fact that the PEIS resistance is much lower at the start of the rest period compared to the stripping resistance at the end of the stripping period confirms that a larger fraction of the interface area is active at the lower 5 μAcm^{-2} current, and this accounts for ΔR.

Next consider the gradual decrease in resistance during the rest period after the initial drop ΔR. The time over which the resistance recovers also provides further insights into the mechanism by which the resistance had risen during stripping. We fitted an exponential function to the temporal change in resistance over each of the rest periods in Fig. 6b; see Fig. S12a. The decay constant τ for all rest periods was in the range 5 min $\leq \tau \leq$ 15 min and had only a weak or no clear dependence on the stripped capacity $C = i_s t$ (Fig. S12b). To further investigate the recovery of resistance, we repeated the strip rest experiments of Figs. 6a and 6b but now with a lower stack pressure of 5 MPa (Fig. 6c) and again extracted decay constants for the recovery of resistance during rest. The range of the measured decay constants from the experiments in Fig. 6b and 6c and additional measurements (Figs. S13a and S13b) with longer stripping and rest periods are all plotted in Fig. 6d as a function of stack pressure (all the measurements are for a stripping current $i_s = 0.6\ \mathrm{mAcm^{-2}}$). The intriguing observation is the negligible dependence of timescale τ upon stack pressure.

The progressive decrease, also termed recovery, of the resistance during each rest period can be rationalised by two possible mechanisms: (i) voids on the interface in pristine Li close by creep under the imposed stack pressure or (ii) the Li creeps through and fills the pores formed in the impurity layer during stripping (Fig. 4c). Can either of these mechanisms explain the negligible dependence of τ on stack pressure? First consider the closure of voids in pristine Li. The calculations in Fig. 3b give the time for void closure (i.e. time t_R at which $V/V_0 \to 0$) and these predictions (for the case of sticking friction) are included in Fig. 6d. A very strong pressure dependence is predicted. Additional calculations with higher Li creep strengths σ_0 (to account for possible size dependence of the strength of Li[32]) are included in Fig. 6d: with increasing σ_0 the predicted recovery time t_R increases but the strong dependence on stack pressure remains unchanged.

Next consider the progressive decrease in resistance during the rest period, as estimated from the impurity layer model. Here recovery time is set by the time for the Li to creep through the gaps $2s \equiv 2(\ell - a)$ between the impurity particles (Fig. 4b). Recall that the increase in resistance is associated with patches on the interface where flow of Li is blocked or rather cannot keep up with the stripping rate (Fig. 5b). In these regions the spacing between impurity particles is $s < s_{\mathrm{cr}} = (\ell_{\mathrm{cr}} - a)$ with ℓ_{cr} given by Eq. (S18) and dependent on the stack pressure and stripping current. The time for Li to creep under the stack pressure through these gaps during the rest period provides an estimate for the time for the resistance to recover. Recall that the critical spacing $s_{\mathrm{cr}} = (\ell_{\mathrm{cr}} - a)$ is a function of the stack pressure and the stripping current i_s such that for $s < s_{\mathrm{cr}}$ the stack pressure cannot force the Li through the gaps between the particles at a rate sufficient to keep up with the imposed stripping current. During the rest period, Li will creep through the gaps and re-establish contact with the electrolyte. The time required for this creep process depends on the spacing of particles: t_{cr} increases with decreasing s. As discussed in the context of Fig. 5b there exists a range of spacings and therefore the time for resistance to recover depends on this distribution of particle spacings. In the absence of information on the distribution of impurity particle spacings, we include in Fig. 6d predictions of the time t_R for Li to creep through gaps of size $s = \alpha s_{\mathrm{cr}}$ for 3 choices of α in the range of 0.5 to unity (Supplementary Section S2.5). Here s_{cr} is calculated from Eq. (S18) as a function of stack pressure p and the stripping current $i_s = 0.6\ \mathrm{mAcm^{-2}}$ used in these experiments. Notwithstanding the fact that there is uncertainty in the distribution of s we observe that t_R has a very weak dependence on stack pressure with the measurements of recovery time suggesting that $0.5 \leq \alpha \leq 0.75$ adequately bounds the measurements. The weak dependence of pressure arises from the two opposing contributions of stack pressure. For a given particle spacing s, the time for Li to creep through the particles decreases with increasing stack pressure; see Eq. (S30). However, given i_s, increasing stack pressure decreases s_{cr} as quantified by Eq. (S31). These two opposing effects result in the weak dependence of t_R stack pressure seen in Fig. 6d.

Current dependent interface resistance associated with impurity deposition

The combined PEIS and direct current measurements of resistance in Figs. 6b and 6c suggest that the resistance of the stripping interface becomes strongly dependent on the stripping current after stripping (due to the accumulation of impurity particles). We now investigate this further by performing strip-rest experiments where we perform two strip-rest cycles at one current and then either increase or decrease the stripping current to directly show the current dependence of resistance. All these experiments are performed with a stack pressure of 10 MPa maintained over all strip and rest cycles.

First consider stripping with $i_s = 0.6\ \mathrm{mAcm^{-2}}$ to a capacity $\sim 6\ \mathrm{mAhcm^{-2}}$ (Fig. 7a). The cell resistance rises from an initial value of $\sim 1.5\ \mathrm{k\Omega}$ to $\sim 8\ \mathrm{k\Omega}$ and then drops back to its initial value during the rest of 4 hrs. The next stripping cycle again at $i_s = 0.6\ \mathrm{mAcm^{-2}}$ but now to a capacity $\sim 0.1\ \mathrm{mAhcm^{-2}}$ shows the resistance again quickly rises to $\sim 8\ \mathrm{k\Omega}$ and drops back to to $\sim 1.5\ \mathrm{k\Omega}$ during the subsequent 5 hr rest period. This clearly shows that after the initial stripping to a capacity $\sim 6\ \mathrm{mAhcm^{-2}}$ the cell resistance at $i_s = 0.6\ \mathrm{mAcm^{-2}}$ is $\sim 8\ \mathrm{k\Omega}$. The next stripping cycle was performed at $i_s = 0.1\ \mathrm{mAcm^{-2}}$ to a capacity $\sim 0.1\ \mathrm{mAhcm^{-2}}$ and now the resistance only rises to $\sim 2\ \mathrm{k\Omega}$ clearly demonstrating that the cell resistance (or rather resistance of the stripping interface) after initial stripping to $\sim 6\ \mathrm{mAhcm^{-2}}$ is current dependent with resistance higher for higher currents. To confirm that this conclusion further we conducted a reverse experiment where we first stripped a fresh cell with $i_s = 0.1\ \mathrm{mAcm^{-2}}$ to a capacity $\sim 7\ \mathrm{mAhcm^{-2}}$ (Fig. 7b). Now the resistance rises much more gradually from the initial value of $\sim 1.8\ \mathrm{k\Omega}$ to only about $\sim 2.5\ \mathrm{k\Omega}$ and subsequent rest-strip cycles (similar to Fig. 7a) at $i_s = 0.1\ \mathrm{mAcm^{-2}}$ confirmed that the cell resistance after stripping to $\sim 7\ \mathrm{mAhcm^{-2}}$ is approximately $2.5\ \mathrm{k\Omega}$ at $i_s = 0.1\ \mathrm{mAcm^{-2}}$. The next strip cycle was conducted at $i_s = 0.6\ \mathrm{mAcm^{-2}}$ to a capacity of $\sim 0.1\ \mathrm{mAhcm^{-2}}$ and the resistance rises rapidly to ~5.5 kΩ confirming that indeed the resistance is higher for higher currents after stripping. The current dependence of the resistance after stripping and the resistance jump ΔR between the stripping cycle and the PEIS measurements during rest are rationalised by noting that ℓ_{cr} is current dependent and a large fraction of the interface is inactive at higher currents since ℓ_{cr} increases with i_s. We note in passing that the immediate rise in resistance upon stripping observed in numerous studies[25,37] might also be related to the current dependence of resistance. For example, given an initial distribution of impurities on the interface (as assumed in this study), the PEIS measurements conducted at low currents prior to stripping will give lower resistances compared to the resistances inferred from the cell voltage immediately on the commencement of stripping.

The above observations have the following features: (i) the cell maintains memory of the loading history; (ii) the time for resistance recovery during a rest period has a negligible dependence on stack pressure and (iii) the resistance after stripping is current dependent. Taken together, these observations add further evidence for our proposed mechanism, viz. contact loss is associated with empty pores between impurity particles deposited or already present on the interface.

Outlook

Commercial lithium metal sources always contain small level of impurities (e.g., the Li used in this study was 99.9% pure). Given that a solid electrolyte allows for the passage of Li ions but not the accompanying solute atoms, insulating particles accumulate on the interface when the Li electrode is stripped. A series of hypothesis-driven experiments associated observations, and theoretical models reveal that deposition of these impurities on the stripping interface is a critical mechanism driving contact loss. Voids or empty pores form within the deposited layer of impurity particles. These voids are mechanically supported by the skeleton of impurity particles and do not collapse under imposed large stack pressures. Our model, based on this mechanism, agrees with the numerous measurements we have reported for a given Li source and our sample of Al-substituted LLZO. But the model also predicts a strong sensitivity of the critical stripping capacity to both the impurities present on the solid electrolyte/Li metal interface at the onset of the experiment (e.g., lithium carbonates and other residual surface impurity phases[33,38]) and the nature (size, concentration, etc.) of the impurities within the Li which get deposited on the interface during stripping.

Our study has focussed on unidirectional stripping to uncover the mechanisms of contact loss during stripping. Under cyclic loading the interpretation of contact loss is more complex. For example, during plating, it may be possible that some impurities deposited on the interface during stripping are driven away from the interface and delay the onset of contact loss in the next stripping phase. But equally, some impurities may stick to the interface[39] prior to cycling and/or accumulate with cycling. In, for example, sulphide-based systems, both impurity formation and its impact, may be further complicated by the chemical reactions that occur between Li metal and the unstable interface with the solid electrolyte. These chemical reactions may again form impurity phases such as Li_2S, Li_3P and LiX (X: halides)[40,41] with lower ionic conductivities than the original electrolyte. Furthermore, different solid-state electrolyte preparation synthesis methods, different dopants and their levels (which all affect the nature and impurity levels)[33,38] and the subsequent methods of making and polishing the pellets will all impact the level of impurities already on the surface of the pellets, affecting the critical capacity and ultimately representing potential sources variability between studies. More studies are needed to understand the effect of cell cycling on contact loss and to explore all of these phenomena including the effect of the Li metal microstructure[42–44] in a wider range of solid electrolytes under both conditions of unidirectional stripping and cycling.

The formation of empty pores of voids associated with impurities deposited during stripping not only rationalises observations of the large stack pressure dependence of the critical capacity and the slow recovery of the interface resistance during a rest period but also provides key insights into the now well-established superior performance of anode-free cells[25] with recent studies[45] showing > 99% efficiency indicating negligible contact loss via void/pore formation. In anode-free cells, the Li anode is created by the plating of Li onto the current collector by passing the Li being stripped from the cathode through the electrolyte. Only Li-ions can pass through the electrolyte and thus the electrolyte serves as a filter creating a very pure Li anode. Our model suggests that anode-free cells have the opportunity of a significantly higher critical capacity. However, the model also suggests that impurities already present at the current collector/solid electrolyte interface play a role in dictating plating mechanics and electrochemistry. Thus, while using high purity Li anodes made for example via the anode-free cell concept may be a key to reducing contact loss in solid-state batteries with Li metal anodes, our work and that of others[46–48] points to the need of experiments to explore more broadly the role of impurity phases in electrochemical performance.

The proposed mechanism of contact loss during stripping is consistent with a wide range of intriguing, and sometimes counterintuitive, measurements that are reported herein. Other mechanisms of contact loss, such as void formation, might also be prevalent in different systems. Further investigations are needed to understand the situations under which the different mechanisms of contact loss dominate.

Acknowledgements

SV and CPG thank the EU for funding via an Advanced EU ERC grant (BATNMR, EC H2020 835073). NAF and VSD acknowledge support by the Faraday Institution grant number FIRG024. JAG and GW thank HVM Catapult for partial funding of the Hydra PFIB at WMG.

References

1. Janek, J., and Zeier, W.G. (2016). A solid future for battery development. Nat. Energy *1*, 16141. https://doi.org/10.1038/nenergy.2016.141.
2. Monroe, C., and Newman, J. (2005). The Impact of Elastic Deformation on Deposition Kinetics at Lithium/Polymer Interfaces. J. Electrochem. Soc. *152*, A396. https://doi.org/10.1149/1.1850854.
3. Janek, J., and Zeier, W.G. (2023). Challenges in speeding up solid-state battery development. Nat. Energy *8*, 230–240. https://doi.org/10.1038/s41560-023-01208-9.
4. Sharafi, A., Meyer, H.M., Nanda, J., Wolfenstine, J., and Sakamoto, J. (2016). Characterizing the Li-$Li_7La_3Zr_2O_{12}$ interface stability and kinetics as a function of temperature and current density. J. Power Sources *302*, 135–139. https://doi.org/10.1016/j.jpowsour.2015.10.053.
5. Kasemchainan, J., Zekoll, S., Spencer Jolly, D., Ning, Z., Hartley, G.O., Marrow, J., and Bruce, P.G. (2019). Critical stripping current leads to dendrite formation on plating in lithium anode solid electrolyte cells. Nat. Mater. *18*, 1105–1111. https://doi.org/10.1038/s41563-019-0438-9.
6. Wang, M.J., Choudhury, R., and Sakamoto, J. (2019). Characterizing the Li-Solid-Electrolyte Interface Dynamics as a Function of Stack Pressure and Current Density. Joule *3*, 2165–2178. https://doi.org/10.1016/j.joule.2019.06.017.
7. Krauskopf, T., Hartmann, H., Zeier, W.G., and Janek, J. (2019). Toward a Fundamental Understanding of the Lithium Metal Anode in Solid-State Batteries - An Electrochemo-Mechanical Study on the Garnet-Type Solid Electrolyte $Li_{6.25}Al_{0.25}La_3Zr_2O_{12}$. ACS Appl. Mater. Interfaces *11*, 14463–14477. https://doi.org/10.1021/acsami.9b02537.
8. Krauskopf, T., Richter, F.H., Zeier, W.G., and Janek, J. (2020). Physicochemical Concepts of the Lithium Metal Anode in Solid-State Batteries. Chem. Rev. *120*, 7745–7794. https://doi.org/10.1021/acs.chemrev.0c00431.
9. Lee, K., Kazyak, E., Wang, M.J., Dasgupta, N.P., and Sakamoto, J. (2022). Analyzing void formation and rewetting of thin in situ-formed Li anodes on LLZO. Joule *6*, 2547–2565. https://doi.org/10.1016/j.joule.2022.09.009.
10. Hatzell, K.B., Chen, X.C., Cobb, C.L., Dasgupta, N.P., Dixit, M.B., Marbella, L.E., McDowell, M.T., Mukherjee, P.P., Verma, A., Viswanathan, V., et al. (2020). Challenges in Lithium Metal Anodes for Solid-State Batteries. ACS Energy Lett. *5*, 922–934. https://doi.org/10.1021/acsenergylett.9b02668.
11. Wang, T., Chen, B., Liu, Y., Song, Z., Wang, Z., Chen, Y., Yu, Q., Wen, J., Dai, Y., Kang, Q., et al. (2025). Fatigue of Li metal anode in solid-state batteries. Science (1979). *388*, 311–316. https://doi.org/10.1126/science.adq6807.
12. Lu, Y., Zhao, C.-Z., Hu, J.-K., Sun, S., Yuan, H., Fu, Z.-H., Chen, X., Huang, J.-Q., Ouyang, M., and Zhang, Q. (2022). The void formation behaviors in working solid-state Li metal batteries. Sci. Adv. *8*, 510. https://doi.org/10.1126/sciadv.add0510.
13. Spencer Jolly, D., Ning, Z., Darnbrough, J.E., Kasemchainan, J., Hartley, G.O., Adamson, P., Armstrong, D.E.J., Marrow, J., and Bruce, P.G. (2020). Sodium/Na β″ Alumina Interface: Effect of Pressure on Voids. ACS Appl. Mater. Interfaces *12*, 678–685. https://doi.org/10.1021/acsami.9b17786.
14. Lewis, J.A., Cortes, F.J.Q., Liu, Y., Miers, J.C., Verma, A., Vishnugopi, B.S., Tippens, J., Prakash, D., Marchese, T.S., Han, S.Y., et al. (2021). Linking void and interphase evolution to electrochemistry in solid-state batteries using operando X-ray tomography. Nat. Mater. *20*, 503–510. https://doi.org/10.1038/s41563-020-00903-2.

15. Roy, U., Fleck, N.A., and Deshpande, V.S. (2021). An assessment of a mechanism for void growth in Li anodes. Extreme Mech. Lett. *46*, 101307. https://doi.org/10.1016/j.eml.2021.101307.
16. Shishvan, S.S., Fleck, N.A., and Deshpande, V.S. (2021). The initiation of void growth during stripping of Li electrodes in solid electrolyte cells. J. Power Sources *488*, 229437. https://doi.org/10.1016/j.jpowsour.2020.229437.
17. Agier, J.A.B., Shishvan, S.S., Fleck, N.A., and Deshpande, V.S. (2022). Void growth within Li electrodes in solid electrolyte cells. Acta Mater. *240*, 118303. https://doi.org/10.1016/j.actamat.2022.118303.
18. Yan, H., Tantratian, K., Ellwood, K., Harrison, E.T., Nichols, M., Cui, X., and Chen, L. (2022). How Does the Creep Stress Regulate Void Formation at the Lithium-Solid Electrolyte Interface during Stripping? Adv. Energy Mater. *12*. https://doi.org/10.1002/aenm.202102283.
19. Shishvan, S.S., Fleck, N.A., McMeeking, R.M., and Deshpande, V.S. (2023). Void growth in metal anodes in solid-state batteries: Recent progress and gaps in understanding. European Journal of Mechanics - A/Solids *100*, 104998. https://doi.org/10.1016/j.euromechsol.2023.104998.
20. Shishvan, S.S., Fleck, N.A., McMeeking, R.M., and Deshpande, V.S. (2023). Vacancy diffusion and its consequences for void growth at the interface of a stripping metal electrode and solid electrolyte. Electrochim. Acta *467*, 143081. https://doi.org/10.1016/j.electacta.2023.143081.
21. Shatzkes, M., and Lloyd, J.R. (1986). A model for conductor failure considering diffusion concurrently with electromigration resulting in a current exponent of 2. J. Appl. Phys. *59*, 3890–3893. https://doi.org/10.1063/1.336731.
22. Clement, J.J., and Lloyd, J.R. (1992). Numerical investigations of the electromigration boundary value problem. J. Appl. Phys. *71*, 1729–1731. https://doi.org/10.1063/1.351204.
23. Rosenberg, R., and Ohring, M. (1971). Void Formation and Growth During Electromigration in Thin Films. J. Appl. Phys. *42*, 5671–5679. https://doi.org/10.1063/1.1659998.
24. Albertus, P., Anandan, V., Ban, C., Balsara, N., Belharouak, I., Buettner-Garrett, J., Chen, Z., Daniel, C., Doeff, M., Dudney, N.J., et al. (2021). Challenges for and Pathways toward Li-Metal-Based All-Solid-State Batteries. ACS Energy Lett. *6*, 1399–1404. https://doi.org/10.1021/acsenergylett.1c00445.
25. Haslam, C.G., Eckhardt, J.K., Ayyaswamy, A., Vishnugopi, B.S., Fuchs, T., Liao, D.W., Dasgupta, N.P., Mukherjee, P.P., Janek, J., and Sakamoto, J. (2025). Evaluating Pressure-dependent Discharge Behavior of Foil Versus In situ Plated Lithium Metal Anodes in Solid-State Batteries. Adv. Energy Mater. *15*. https://doi.org/10.1002/aenm.202403614.
26. Roach, A.M., Zhu, W., Vema, S., McMeeking, R.M., Grey, C.P., Deshpande, V.S., and Fleck, N.A. (2025). Void growth in the lithium anode of a solid state battery. European Journal of Mechanics, A/Solids *113*. https://doi.org/10.1016/j.euromechsol.2025.105710.
27. Ortmann, T., Burkhardt, S., Eckhardt, J.K., Fuchs, T., Ding, Z., Sann, J., Rohnke, M., Ma, Q., Tietz, F., Fattakhova-Rohlfing, D., et al. (2023). Kinetics and Pore Formation of the Sodium Metal Anode on NASICON-Type $Na_{3.4}Zr_2Si_{2.4}P_{0.6}O_{12}$ for Sodium Solid-State Batteries. Adv. Energy Mater. *13*. https://doi.org/10.1002/aenm.202202712.
28. Fuchs, T., Ortmann, T., Becker, J., Haslam, C.G., Ziegler, M., Singh, V.K., Rohnke, M., Mogwitz, B., Peppler, K., Nazar, L.F., et al. (2024). Imaging the microstructure of

lithium and sodium metal in anode-free solid-state batteries using electron backscatter diffraction. Nat. Mater. *23*, 1678–1685. https://doi.org/10.1038/s41563-024-02006-8.
29. Masias, A., Felten, N., Garcia-Mendez, R., Wolfenstine, J., and Sakamoto, J. (2019). Elastic, plastic, and creep mechanical properties of lithium metal. J. Mater. Sci. *54*, 2585–2600. https://doi.org/10.1007/s10853-018-2971-3.
30. Fincher, C.D., Ojeda, D., Zhang, Y., Pharr, G.M., and Pharr, M. (2020). Mechanical properties of metallic lithium: from nano to bulk scales. Acta Mater. *186*, 215–222. https://doi.org/10.1016/j.actamat.2019.12.036.
31. Masias, A., Felten, N., and Sakamoto, J. (2021). Characterizing the mechanical behavior of lithium in compression. J. Mater. Res. *36*, 729–739. https://doi.org/10.1557/s43578-020-00028-x.
32. Stallard, J.C., Vema, S., Grey, C.P., Deshpande, V.S., and Fleck, N.A. (2023). The strength of a constrained lithium layer. Acta Mater. *260*, 119313. https://doi.org/10.1016/j.actamat.2023.119313.
33. Vema, S., Sayed, F.N., Nagendran, S., Karagoz, B., Sternemann, C., Paulus, M., Held, G., and Grey, C.P. (2023). Understanding the Surface Regeneration and Reactivity of Garnet Solid-State Electrolytes. ACS Energy Lett. *8*, 3476–3484. https://doi.org/10.1021/acsenergylett.3c01042.
34. Barai, P., Fuchs, T., Trevisanello, E., Richter, F.H., Janek, J., and Srinivasan, V. (2024). Study of Void Formation at the Lithium|Solid Electrolyte Interface. Chemistry of Materials *36*, 2245–2258. https://doi.org/10.1021/acs.chemmater.3c01708.
35. Eckhardt, J.K., Klar, P.J., Janek, J., and Heiliger, C. (2022). Interplay of Dynamic Constriction and Interface Morphology between Reversible Metal Anode and Solid Electrolyte in Solid State Batteries. ACS Appl. Mater. Interfaces *14*, 35545–35554. https://doi.org/10.1021/acsami.2c07077.
36. Eckhardt, J.K., Fuchs, T., Burkhardt, S., Klar, P.J., Janek, J., and Heiliger, C. (2022). 3D Impedance Modeling of Metal Anodes in Solid-State Batteries–Incompatibility of Pore Formation and Constriction Effect in Physical-Based 1D Circuit Models. ACS Appl. Mater. Interfaces *14*, 42757–42769. https://doi.org/10.1021/acsami.2c12991.
37. Schall, T.A., Fuchs, T., Eckhardt, J.K., Klunz, T., Mogwitz, B., Sann, J., Peppler, K., and Janek, J. (2025). Evolution of Pore Volume During Stripping of Lithium Metal in Solid-State Batteries Observed with Operando Dilatometry. Small *21*. https://doi.org/10.1002/smll.202505053.
38. Berge, A.H., Vema, S., O'Keefe, C.A., and Grey, C.P. (2025). Locating Impurity Phases in the Lithium-Ion Conductor Al-Doped Li7La3Zr2O12 through Dynamic Nuclear Polarization and Nuclear Magnetic Resonance Spectroscopy. Chemistry of Materials *37*, 3842–3852. https://doi.org/10.1021/acs.chemmater.5c00807.
39. Harry, K.J., Hallinan, D.T., Parkinson, D.Y., MacDowell, A.A., and Balsara, N.P. (2014). Detection of subsurface structures underneath dendrites formed on cycled lithium metal electrodes. Nat. Mater. *13*, 69–73. https://doi.org/10.1038/nmat3793.
40. Narayanan, S., Ulissi, U., Gibson, J.S., Chart, Y.A., Weatherup, R.S., and Pasta, M. (2022). Effect of current density on the solid electrolyte interphase formation at the lithium|Li6PS5Cl interface. Nat. Commun. *13*, 7237. https://doi.org/10.1038/s41467-022-34855-9.
41. Alt, C.D., Müller, N.U.C.B., Riegger, L.M., Aktekin, B., Minnmann, P., Peppler, K., and Janek, J. (2024). Quantifying multiphase SEI growth in sulfide solid electrolytes. Joule *8*, 2755–2776. https://doi.org/10.1016/j.joule.2024.07.006.
42. Singh, D.K., Fuchs, T., Krempaszky, C., Mogwitz, B., Burkhardt, S., Richter, F.H., and Janek, J. (2023). Overcoming Anode Instability in Solid-State Batteries through

Control of the Lithium Metal Microstructure. Adv. Funct. Mater. *33*. https://doi.org/10.1002/adfm.202211067.

43. Fuchs, T., Ortmann, T., Becker, J., Haslam, C.G., Ziegler, M., Singh, V.K., Rohnke, M., Mogwitz, B., Peppler, K., Nazar, L.F., et al. (2024). Imaging the microstructure of lithium and sodium metal in anode-free solid-state batteries using electron backscatter diffraction. Nat. Mater. *23*, 1678–1685. https://doi.org/10.1038/s41563-024-02006-8.
44. Self, E., Tsai, W.-Y., Lin, Y.-R., Fuchs, T., Owensby, K., Lerch, C., Burberg, S., Browning, K., Herbert, E., Chen, X., et al. (2025). Is all lithium created equal? Effects of processing conditions on lithium microstructure and battery performance. Preprint, https://doi.org/10.26434/chemrxiv-2025-pjttm https://doi.org/10.26434/chemrxiv-2025-pjttm.
45. Liao, D.W., Zeng, D., Mishra, G.K., Lee, S.Y., Melemed, A.M., Penley, D., Iwamura, R., Kawakami, H., Aihara, Y., Aotani, K., et al. (2025). Solid-Gas Interphase Formation in Anode-Free Solid-State Batteries. J. Am. Chem. Soc. *147*, 48013–48027. https://doi.org/10.1021/jacs.5c13252.
46. Becker, J., Weintraut, T., Benz, S.L., Fuchs, T., Lerch, C., Becker, P., Eckhardt, J.K., Henß, A., Richter, F.H., and Janek, J. (2025). Purity of lithium metal electrode and its impact on lithium stripping in solid-state batteries. Nat. Commun. *16*, 5395. https://doi.org/10.1038/s41467-025-61006-7.
47. Yoon, S.G., Vishnugopi, B.S., Nelson, D.L., Yong, A.X. Bin, Wang, Y., Sandoval, S.E., Thomas, T.A., Cavallaro, K.A., Shevchenko, P., Alsaç, E.P., et al. (2025). Interface morphogenesis with a deformable secondary phase in solid-state lithium batteries. Science (1979). *388*, 1062–1068. https://doi.org/10.1126/science.adt5229.
48. Mann, M., Schwab, C., dos Santos, L.C.P., Spatschek, R., Fattakhova-Rohlfing, D., and Finsterbusch, M. (2025). Improving the rate performance of lithium metal anodes: In-situ formation of 3D interface structures by mechanical mixing with sodium metal. Energy Storage Mater. *74*, 103975. https://doi.org/10.1016/j.ensm.2024.103975.

Methods

Manufacture of LLZO

Doped LLZO ($Al_{0.36}Li_{5.92}La_3Zr_2O_{12}$) was synthesised by a conventional solid-state synthesis route by mixing precursors (La_2O_3, ZrO_2, Li_2CO_3 (with 10% excess), and Al_2O_3) and heating the mixture to 1000 °C for 6 hrs under flowing O_2 in a MgO crucible[33]. The synthesized powders were stored in airtight vials to minimise exposure to ambient air. The doped LLZO powder was hot-pressed at 1080-1085 °C for 75 mins under 62 MPa using a custom built hot-press and cut into 1-1.3 mm thick discs[33]. The phase purity of the pellets was confirmed using powder X-ray diffraction (Fig. S14) and the porosity was estimated from density measurements to be < 1%. The hot-pressed pellets had a grain size of $\sim 4 - 10$ μm.

Cell assembly and measurements of interface resistance

The LLZO pellets were successively dry polished with increasing grit number sandpapers (1200, 2500, 4000) and finally wet polished with an oil-based 1 μm diamond suspension. The pellets were immediately cleaned with dry acetone and transferred to an Argon glovebox to avoid prolonged exposure to air. In the glovebox, the pellets were sealed in a custom-made quartz tube. The sealed tube was then heated at the rate of 10°C min^{-1} to 500 °C for 1 hour under flowing gas (2:1 ratio of oxygen to argon) in a furnace outside the glovebox. Subsequently, the quartz tube was purged with argon and transferred back to the glovebox within 25 minutes, without any exposure to air[33].

To assemble a cell, a Li metal chip (15.6 mm diameter and 250 μm thick, PI-KEM) was gently scraped multiple times with a SS316 spatula until both surfaces of the chip were shiny. This cleaning step was performed on Kapak® pouch bags (300-0306, VWR) with special care taken to avoid Li metal contact with any other surface. The Li metal chip was placed on top of a pouch bag and rolled to reduce its thickness to below 100 μm using a polished stainless steel SS316 rod. The rolled Li metal surface in contact with SS316 rod was again scraped with a spatula. The rolled lithium metal was gently lifted from the pouch bag surface and placed on top of a polished SS316 plate (mirror finish) such that the lithium metal surface in contact with plastic pouch bag was now facing upwards away from the SS316 steel plate and this face was again scraped. Li metal discs were punched out from the thinned lithium metal on a SS316 plate. Cells were assembled by sticking punched polished Li metal discs on both sides of the heat-treated pellets. The entire assembly (Li - Doped LLZO - Li) was heated at 190 °C for 5 mins in tantalum crucibles (EVCEB-6MMO, Kurt J. Lesker) to melt the lithium. The area of the Li electrodes was observed to shrink upon melting the Li metal and the interface area was estimated from photos of each cell captured via a camera inside the glovebox (a Dino-Lite digital microscope camera (AM7115MZTL, GT Vision Ltd.). The cells were then closed in Swagelok cells for further testing.

Cells were subject to different galvanostatic cycling conditions inside the glovebox using a VSP-300 Biologic cycler (where the current for the required interface current density $\mathrm{i_s}$ was estimated from the area of the Li-LLZO interface as determined from the images). To apply the stack pressure, one side of Swagelok cell was loosened, and the cell was positioned within a screw-driven test machine inside the glovebox. A constant force on the cell was maintained throughout the electrochemical testing protocol. Potentiostatic Electrochemical Impedance Spectroscopy (PEIS) using a 10 mV amplitude and frequency sweep from 7 MHz to 1 Hz was conducted just before electrochemical testing of each cell to estimate the interface resistance). The PEIS spectra of each cell were fit with an equivalent circuit diagram (Fig. S15) using custom written codes in Python to extract the combined interfacial resistance ($R_{\mathrm{interface}}$) of both interfaces. The effective interface resistance Z was calculated by accounting for the different electrode diameters (Supplementary S3). After the electrochemical test finished, the cell was immediately taken out of Swagelok and interface areas again determined by taking images of the electrodes as described above. The cell capacities were normalised by the final stripping interface area to account for the area change during testing under load.

For the strip-rest-strip cycle experiments, the cell resistance during the galvanostatic step (stripping) was estimated by dividing the cell voltage by current applied. For the PEIS measurements during the rest step, we used the same protocol as that for the pristine cell. Representative spectra are included in Fig. S16 over selected rest periods for the data in Fig. 6a. The real part of impedance spectrum at 20 Hz was used as an approximation for the total cell resistance R (Supplementary S3) and this resistance during rest periods is plotted in Figs. 6b-c and Figs. 7a-b.

Cryo- PFIB SEM observations

The tested cells (pellets) were fractured into two pieces inside a glovebox to expose the cross-section of the electrodes for analysis. One of the fractured pieces was mounted onto an SEM stub, and copper strips were affixed to the electrode, extending from its surface to the sides of the stub. This was performed to reduce charging effects during EDS mapping. The stub containing the sample was then transported to the Thermo-Fisher Scientific Helios 5 Hydra PFIB system using a CleanConnect inert gas transfer module to preserve its pristine condition. Once inside the system, the sample was cooled to -150 °C and subjected to successive milling using an Ar-ion beam. Initial milling was performed at a 4 μA current to expose the interface and eliminate surface artifacts that could have formed during sample transfer, glovebox exposure, or from residual overhang resulting from the fracture event. The cross-section was refined through a series of milling steps with progressively lower currents (2 μA, 400 nA, 140 nA, and 14 nA) to remove terracing effects. Finally, a polishing step was carried out using a 7 nA current to mitigate curtaining effects and achieve a smooth cross-sectional surface. High-resolution SEM images were collected at different spots using a 2 kV 200pA electron beam with secondary electron (SE) detectors (TLD and ICE) in the Hydra SEM. EDS maps were recorded at 5 keV at locations of interest using an Oxford Instruments Ultim Max 170 detector.

Figures

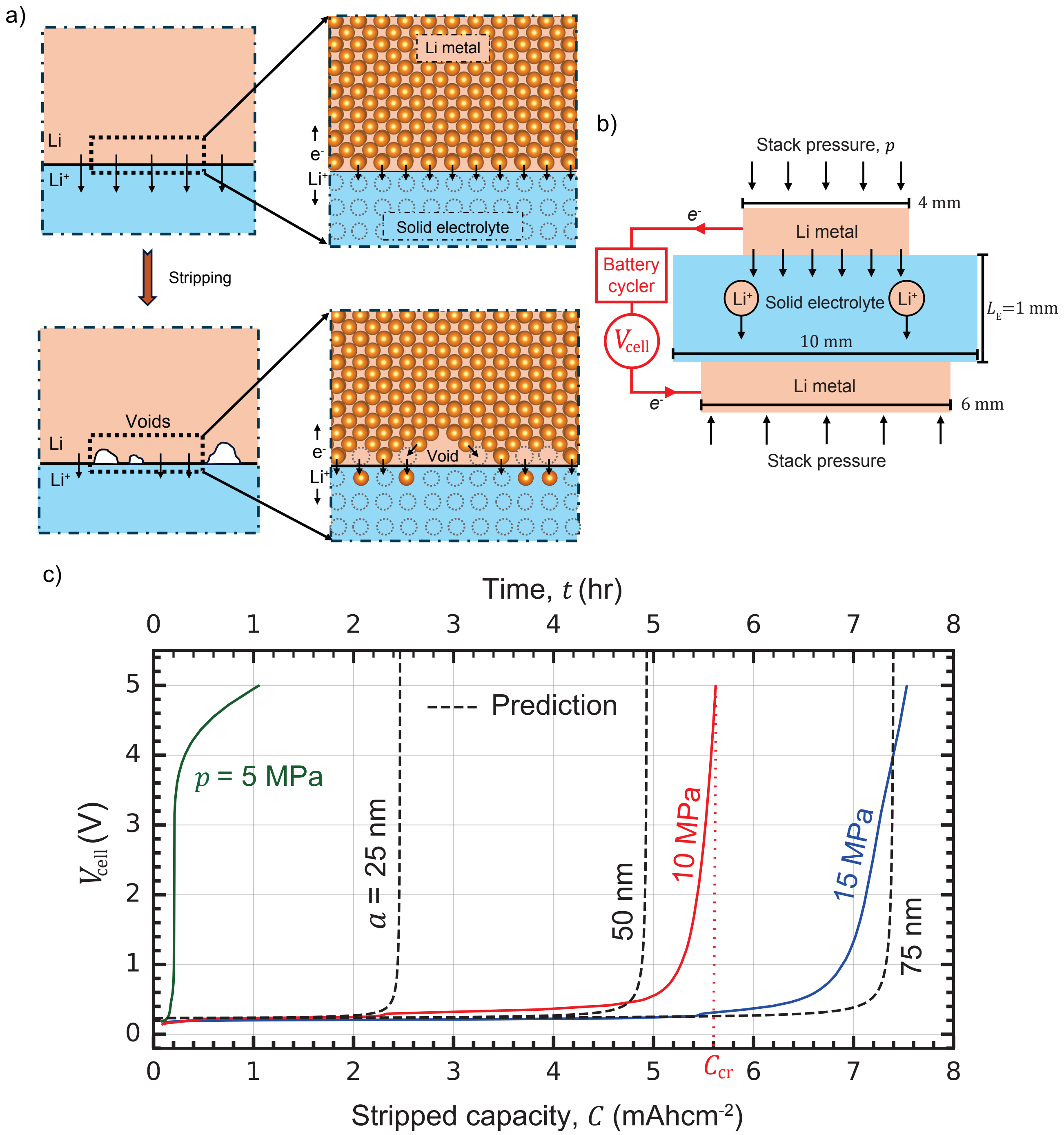

Figure 1: Contact loss during stripping. (a) Sketch of a void growth mechanism that is commonly assumed to be the cause of contact loss on the stripping interface. Lithium (shown as brown balls) is stripped from the Li metal electrode and voids are thought to grow at the electrode/electrolyte interface resulting in contact loss between the electrode and electrolyte. (b) Schematic of the mechanical and electrical loading of the Li/LLZO/Li cell. Note the different electrode areas on the plating and stripping interfaces of the cell. (c) Temporal evolution of cell voltage for cells with interface resistances $Z \approx 9\ \Omega\text{cm}^2$ and an imposed stripping current $i_s = 1\ \text{mAcm}^{-2}$. Measurements are shown for three imposed stack pressures p with the data plotted with time t parametrised by capacity $C \equiv i_s t$ (the upper x-axis shows the scale in units of time). Predictions using equation (2) are also included for a volume fraction $f = 0.1\%$ of impurity particles with three different radii a in the Li electrode.

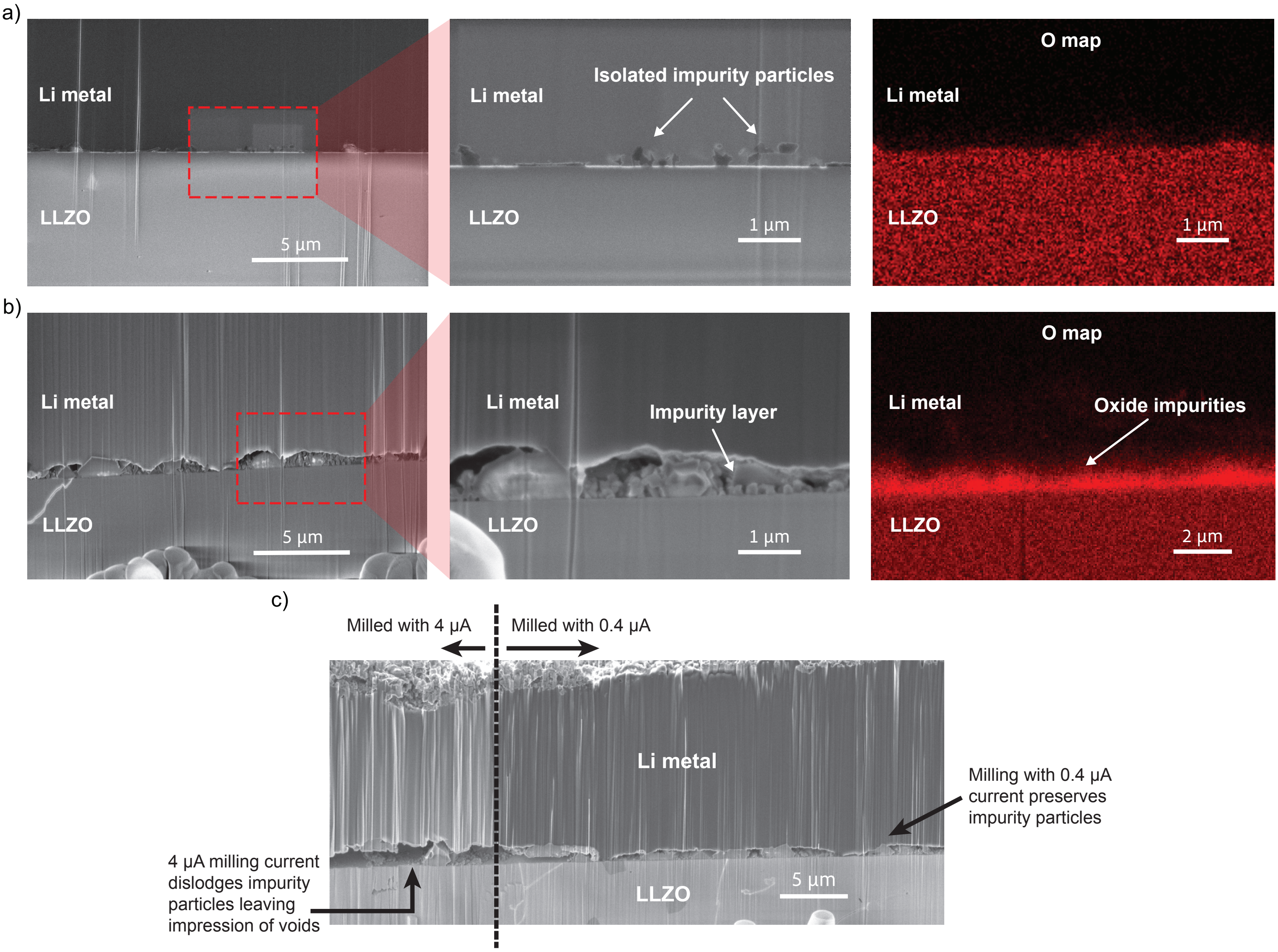

Figure 2: Observations of the stripped interface. Cryo-PFIB-SEM images of the interface of a cell with $Z \approx 9\ \Omega\text{cm}^2$ in the (a) pristine state (i.e., prior to galvanostatic testing), (b) the stripping interface after stripping at $i_s = 1\ \text{mAcm}^{-2}$ with a stack pressure 10 MPa. The images correspond to the $p = 10$ MPa cell in Fig. 1c and are taken after the cell voltage has risen to 5 V. The images are shown at two levels of magnification (higher magnification indicated by the red dashed boxes) and include Oxygen EDS maps to show the elemental composition at the interface. (c) The stripping interface of the $p = 10$ MPa cell in Fig. 1c after the voltage has risen to 5V. Different portions of the cross-section have been milled used different milling currents and the image shows that a high milling current disturbs (and dislodges) the impurity particles from the interface giving the impression of the presence of voids in the Li at the stripping interface. We propose that the voids seen upon stripping in previous studies[12,28] could have been created by the high milling currents used during cross-sectioning.

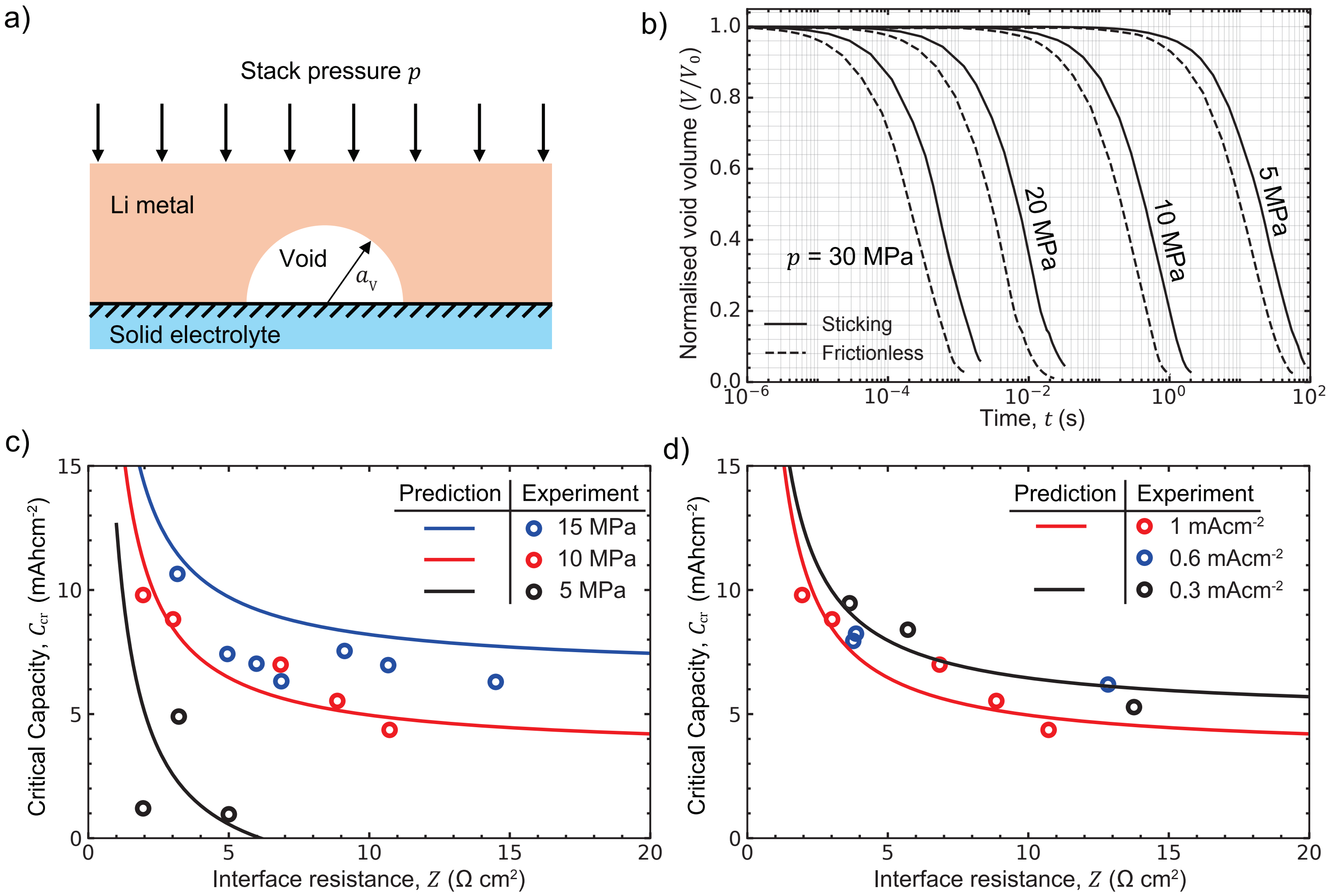

Figure 3: Contact loss during stripping under imposed stack pressure. (a) Sketch of a hemispherical void with radius a_v in a large Li electrode subjected to a stack pressure p. (b) Predictions of the temporal evolution (time $t = 0$ at the instant of the application of pressure) of the normalised void volume V/V_0, where V_0 is the initial void volume for selected imposed stack pressures p. Predictions are shown for free-sliding and sticking friction boundary conditions between the Li and the rigid interface. Summary of the critical capacity C_{cr} electrochemical measurements (circles) plotted as a function of cell interface resistance Z for (c), an imposed current $i_s = 1$ mAcm^{-2} and three values of stack pressure and (d), an imposed stack pressure $p = 10$ MPa and selected values of current i_s. Predictions of C_{cr} based on the impurity deposition model with a single layer of impurity particles are included in (c) and (d) (lines). The predictions here are for a given Li source and thus a fixed set of impurity parameters. The sensitivity of the predictions to the impurity parameters is shown in Figs. S9.

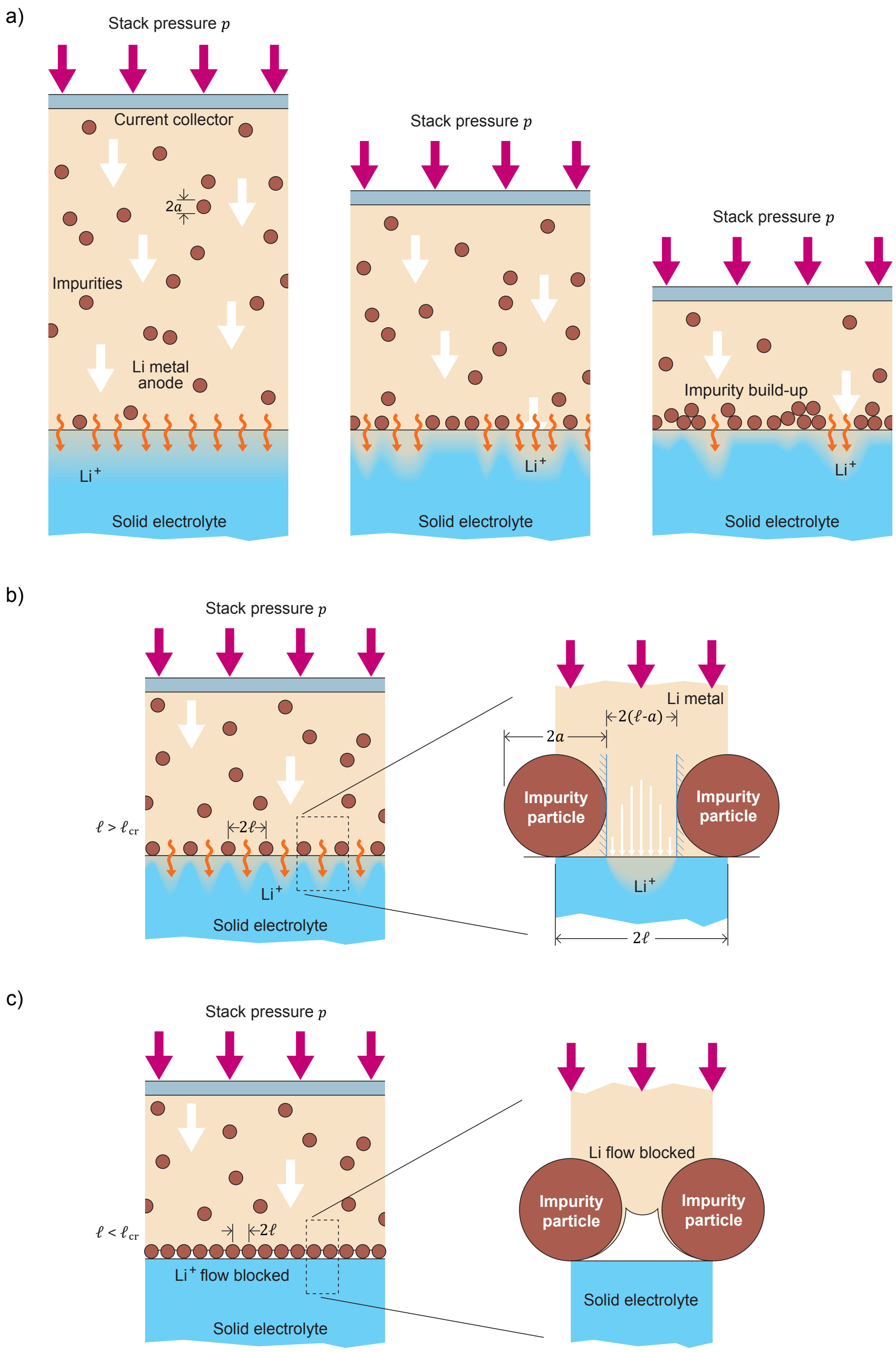

Figure 4: Schematics of the impurity deposition mechanism. (a) Impurities of radius a within the electrode advect with the thinning electrode and deposit on the interface. Continued stripping increases the density of these solutes on the interface with the deposits existing as a single layer in places and multiple layers in other locations. (b) Sketch of our model comprising a single layer of uniformly spaced impurities at the interface. The zoom-in show particles spaced at $\ell > \ell_{\mathrm{cr}}$ such that the stack pressure that is sufficient to creep the Li through the gaps between the particles with the flow of Li between the particles approximated as flow through a pipe. (c) As the particle spacing decreases to $\ell \leq \ell_{\mathrm{cr}}$, the stripping rate exceeds creep rate of the Li through the gaps under the imposed stack pressure and empty pores/voids form. This inhibits further stripping. The blockage of Li is shown in the zoom-in which also emphasizes that a thin Li layer remains adhered to the impurity particles providing a pathway for electrons.

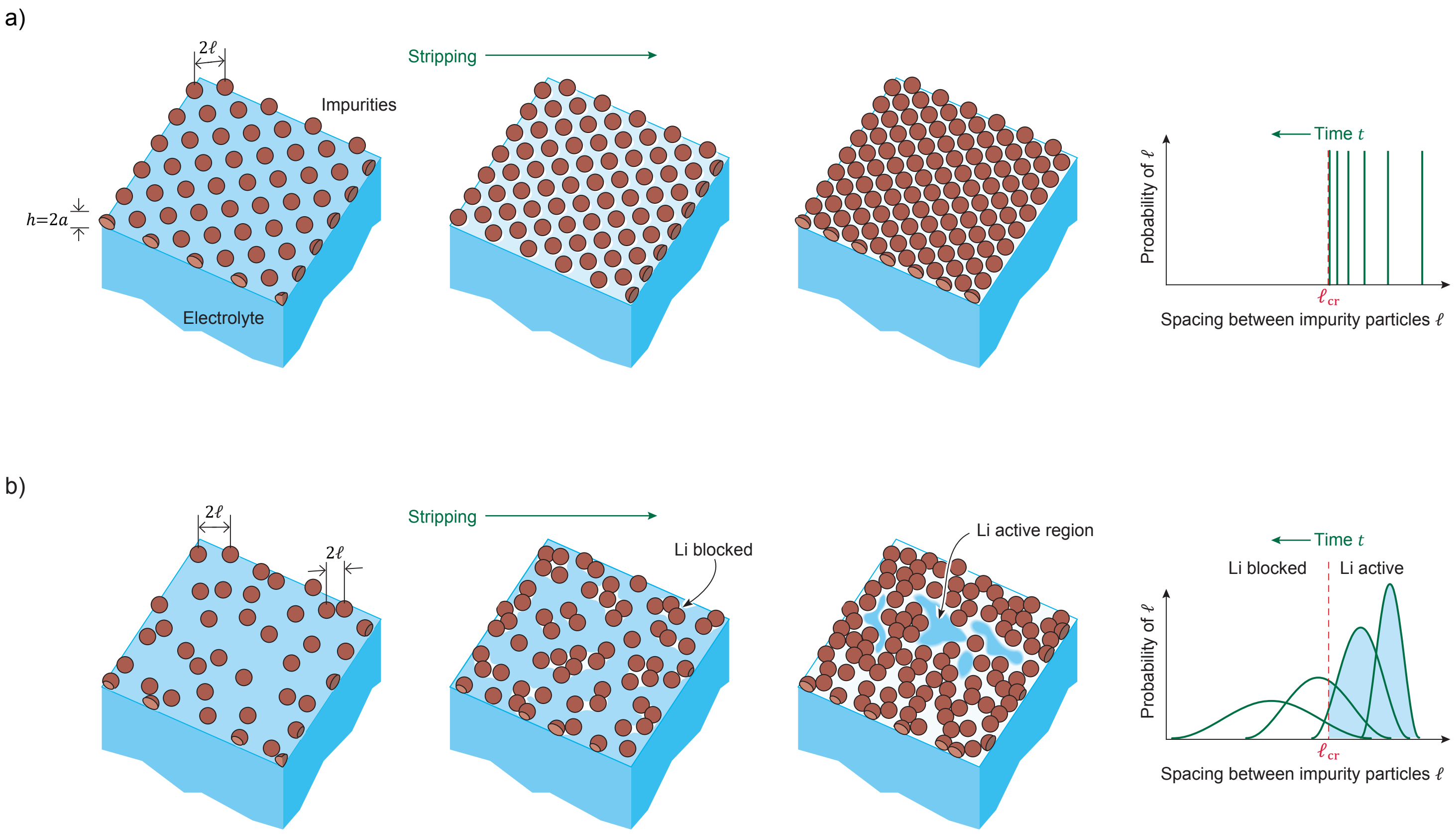

Figure 5: Uniform versus non-uniform deposition of impurities. (a) Sketches of the evolution of the uniformly spaced impurities on the interface. The temporal evolution of the probability density of the spacing ℓ of the particles on the interface is also included. The uniform spacing implies that the probability density is a dirac delta function in $(\ell - \ell_t)$ where ℓ_t is the current spacing at time t. (b) Sketches of the evolution of the non-uniform deposition of the impurity particles on the interface. The probability density of the spacing ℓ evolves such that not only does the mean particle spacing decrease, but the standard deviation of the distribution also increases. As a consequence, the cumulative probability of spacings $\ell < \ell_{\mathrm{cr}}$ increases with time and these become inactive regions of the interface. The inactive regions are marked in the sketches.

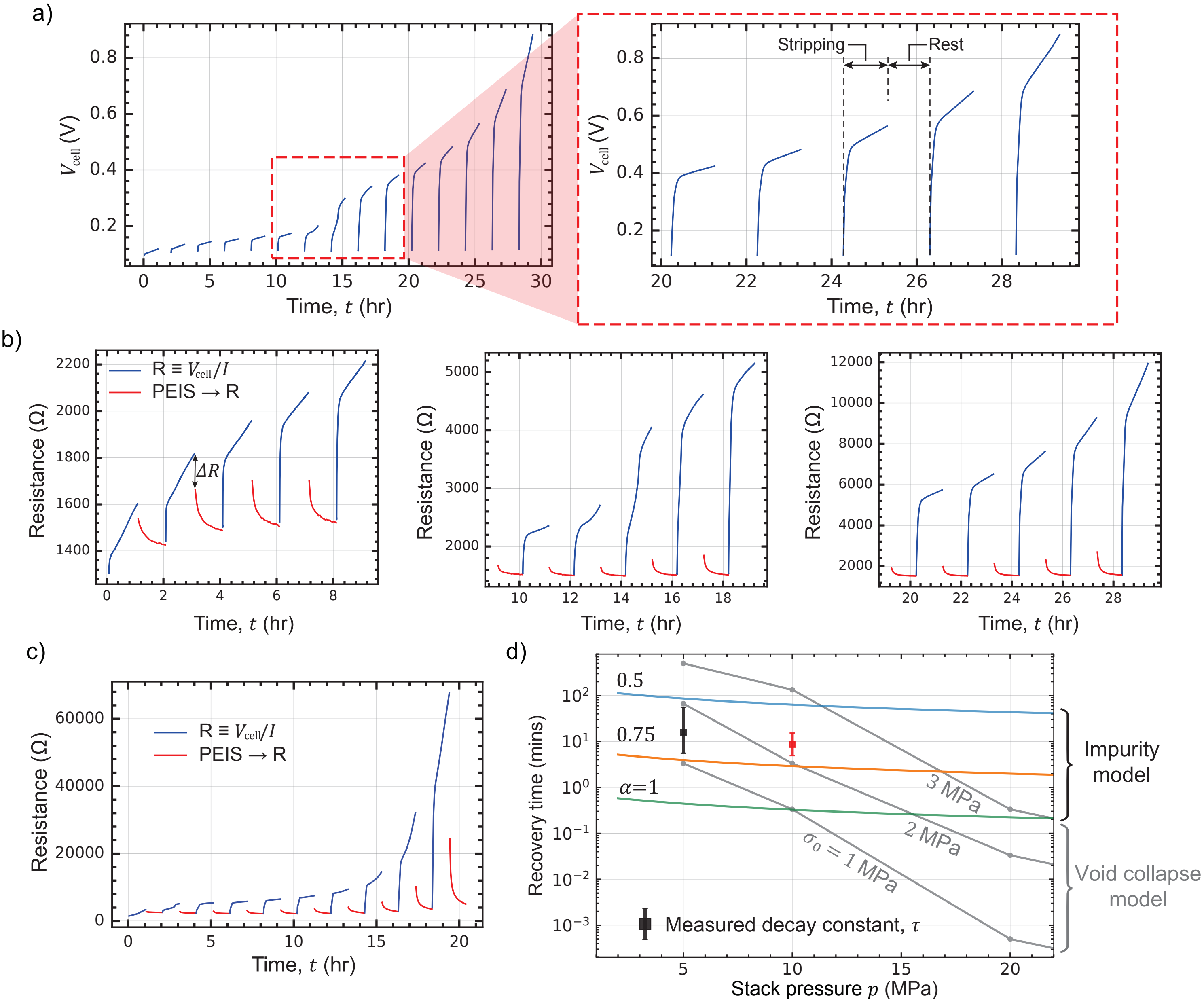

Figure 6: Recovery of resistance during rest after stripping. (a) The measured cell voltage V_{cell} as a function of time t for strip-rest cycles with a period of 2 hrs under the application of a stack pressure $p = 10$ MPa and stripping current $i_s = 0.6\ \mathrm{mAcm^{-2}}$ (interface resistance $Z \approx 8\ \Omega\mathrm{cm}^2$). The inset shows a zoom-in over the period t~20 hrs to 30 hrs. (b) The corresponding cell resistance R versus time t. The resistance during galvanostatic stripping is defined as $R \equiv V_{\mathrm{cell}}/I$ where V_{cell} is the cell voltage and I the imposed current while the resistance during the rest period obtained is via PEIS measurements. The resistance jump ΔR between the end of the stripping period and the start is the rest period is indicated. (c) A repeat of the experiment in (a) and (b) with a stripping current of $i_s = 0.6\ \mathrm{mAcm^{-2}}$ but a stack pressure of $p = 5$ MPa. The data is shown in the form of $R \equiv V_{\mathrm{cell}}/I$ versus time t over the stripping and rest periods. (d) Comparison between measurements of the time τ for the resistance to recover during rest and corresponding predictions. Predictions are shown for the time t_{cr} voids to close for a range of choices of the Li creep strength σ_0 and the time for Li to creep through pores between impurity particles for a range of choices of particle spacings $s = \alpha s_{\mathrm{cr}}$. The weak dependence of the recovery time τ on stack pressure is only captured by the impurity particle model.

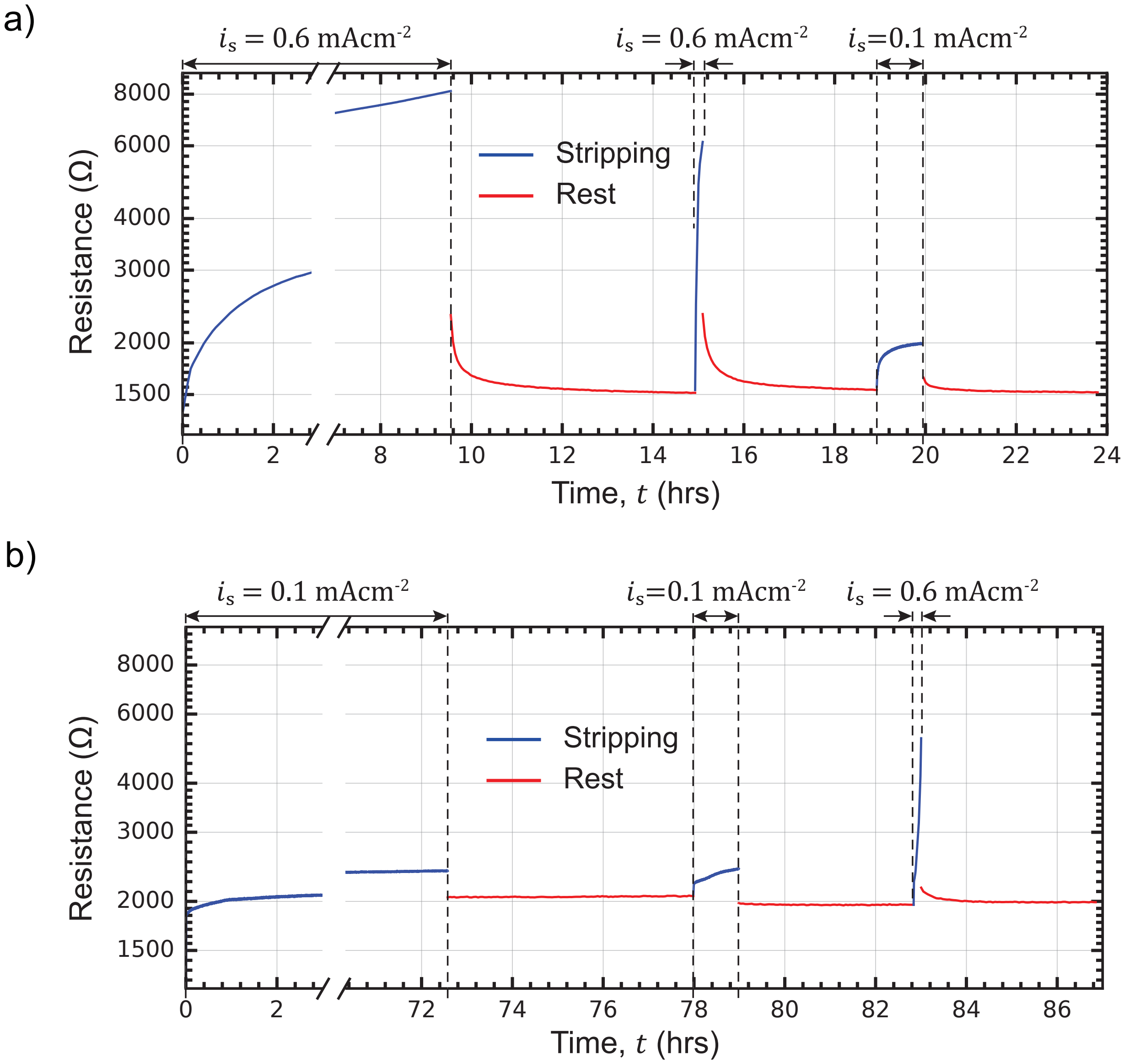

Figure 7: Current dependence of interface resistance after stripping. Strip-rest cycles at (a) $i_s = 0.6\ \mathrm{mAcm}^{-2}$ followed by $i_s = 0.1\ \mathrm{mAcm}^{-2}$ and the reverse with (b) $i_s = 0.1\ \mathrm{mAcm}^{-2}$ followed by $i_s = 0.6\ \mathrm{mAcm}^{-2}$ both under stack pressure of $p = 10$ MPa.

Contact loss in all solid-state Li-ion batteries via deposition of impurities

Sundeep Vema[1,2], James A. Gott[3], Hao Yin[4], Ashley M. Roach[4], Geoff West[3], Norman A. Fleck[4], Vikram S. Deshpande[4,*] and Clare P. Grey[1,2,*]

[1] Yusuf Hamied Department of Chemistry, University of Cambridge, Lensfield Road, Cambridge, CB2 1EW, United Kingdom
[2] The Faraday Institution, Quad One, Harwell Campus, Didcot, OX11 0RA, United Kingdom
[3] Warwick Manufacturing Group (WMG), University of Warwick, Coventry, CV4 7AL, United Kingdom
[4] Department of Engineering, University of Cambridge, Trumpington Street, Cambridge, CB2 1PZ, United Kingdom

Supporting Information

Supplementary Section S1: Numerical calculations of void collapse under stack pressure
Supplementary Section S2: Derivation of flow through the porous interface layer
Supplementary Section S3: Calculation of the interface resistance Z in the Li/LLZO/Li cells with different electrode areas
Supplementary References
Supplementary Figures S1-S18

S1: Numerical calculations of void collapse under stack pressure

The hemispherical void collapse calculations of Fig. 3b were performed using the Multiphysics software COMSOL®. The problem under consideration is sketched in Fig. 3a (and repeated in Fig. S17a).

S1.1 Non-linear viscous creep response of Li and the governing mechanical equations

In line with an extensive literature[1–3] on the mechanical properties of Li at room temperature, we model Li as an incompressible creeping solid. For realistic creep rates in the Li/LLZO/Li cells, dislocation creep dominates in Li with the stress and strain-rate related by a power-law relationship. In terms of a reference stress σ_0 and reference strain-rate $\dot{\varepsilon}_0$ we define a dissipation potential for the Li as

$$\Phi_\mathrm{m} \equiv \frac{\sigma_0 \dot{\varepsilon}_0}{n+1}\left(\frac{\dot{\varepsilon}}{\dot{\varepsilon}_0}\right)^{N+1}, \tag{S1}$$

where N is the power-law exponent and $\dot{\varepsilon} \equiv \sqrt{(2/3)\dot{\varepsilon}_{ij}\dot{\varepsilon}_{ij}}$ is the von-Mises effective strain-rate in terms of the incompressible strain-rate $\dot{\varepsilon}_{ij}$ (i.e. $\dot{\varepsilon}_{kk} = 0$). The power law creep properties of Li are well-established in the literature[1–3] with $\sigma_0 = 1$ MPa, $\dot{\varepsilon}_0 = 0.01\ \mathrm{s}^{-1}$ and $n = 1/N = 6.6$.

For this incompressible solid, the incompressible strain-rate $\dot{\varepsilon}_{ij}$ is related to the deviatoric stress $S_{ij} \equiv \sigma_{ij} - (\sigma_{kk}/3)\delta_{ij}$, written in terms of the Cauchy stress σ_{ij} and the Kronecker delta δ_{ij}, via

$$S_{ij} \equiv \frac{\partial \Phi_\mathrm{m}}{\partial \dot{\varepsilon}_{ij}}. \tag{S2}$$

The Li in the electrode satisfies static stress equilibrium $\sigma_{ij,j} = 0$, where the comma denotes the spatial derivative with the repeated suffix follows the usual convention and the velocity field v_i is divergence-free, i.e., $v_{i,i} = 0$. The strain rate $\dot{\varepsilon}_{ij} \equiv 0.5(v_{i,j} + v_{j,i})$ and the deviatoric stress are related via (S1) and (S2) with the hydrostatic stress σ_{kk} solved as a Lagrange multiplier to enforce incompressibility $\dot{\varepsilon}_{kk} = 0$. These governing equations together are referred to as the nonlinear Stokes equations.

S1.2 The boundary value problem

Consider an electrode under a stack pressure p with the electrode assumed to be large compared to the initial void radius a_v. Thus, for numerical convenience we analyse a hemispherical region of radius $\mathcal{R} \gg a_\mathrm{v}$ centred at the centre of the hemispherical void as shown in Fig. S17b. The electrode/electrolyte interface is located at $z = 0$ and modelled as a rigid surface. On the surface $z = 0$, we set the vertical component of velocity to vanish, $v_z = 0$ to ensure that Li cannot penetrate through the solid electrolyte under the imposition of only stack pressure. On the hemispherical surface $\mathcal{R}$, a stack pressure p is imposed via traction boundary conditions while the void surface is assumed to be traction free. Two extremes of friction condition are considered for the interaction of the electrode with the rigid surface $z = 0$: (i) frictionless sliding of the Li such that the radial traction $T_r = 0$ and (ii) sticking friction such that Li material points in contact with $z = 0$ have a vanishing radial velocity $v_r = 0$. Pressure was applied at time $t = 0$ and the solution provides the evolution of the void shape with time.

Solutions of the nonlinear Stokes flow equations with the above boundary conditions were obtained using the Multiphysics software COMSOL®. A regular mesh is needed in the Li for resolving the flow fields. To maintain the quality of the mesh during the void collapse, we employ a feature called "moving mesh" in the Multiphysics software COMSOL®. With this feature enabled, the solution technique used in the electrode is akin to an Arbitrary Lagrangian-Eulerian (ALE) description, which is capable of coping with the large distortion of the Li.

S1.3 Brief description of numerical results

The predictions of void size and shape with increasing time for an imposed stack pressure $p = 10$ MPa and the choice $a_\mathrm{v} = 25$ µm are included in Figs. S2a and S2b for frictionless and sticking boundary conditions, respectively (time $t = 0$ at the instant the pressure is first applied). The images in Fig. S4 show the void evolution along with spatial distributions of the von-Mises stress $\sigma \equiv \sqrt{(3/2)S_{ij}S_{ij}}$. The corresponding temporal evolutions of the void volume are included in Fig. 3b where V is the current void volume at time t and $V_0 = (2/3)\pi a_\mathrm{v}^3$. The void collapses slightly faster if frictionless boundary conditions are assumed. While the void collapses in approximately a self-similar manner in case the frictionless interface case, the void changes shape continuously when sticking friction is imposed.

S2: Derivation of flow through the porous interface layer

Consider the interface layer comprising of impurity particles deposited on the interface as shown in Fig. 4. The Li is driven through the layer by the applied stack pressure and we consider two limiting cases to derive a relation between the steady flow rate of Li through the layer and the applied pressure p: (i) the case of a thick layer when the layer thickness $h \gg a$ where a is the impurity particle radius and (ii) a single incomplete monolayer of impurity particles such that $h = 2a$. In both cases and consistent with the known creep response of Li we treat Li as a non-linear viscous solid.

S2.1 Flow of a non-linear viscous fluid through a circular pipe

Flow of a fluid through a porous medium is usually idealised by the steady flow of a liquid through a cylindrical pipe of radius R. For simplicity in the context of the shear flow of the fluid through the pipe we rewrite the creep constitutive relations (S1) and (S2) in terms of the shear stress τ and shear strain rate $\dot{\gamma}$ as

$$\tau = \tau_0 \left(\frac{\dot{\gamma}}{\dot{\gamma}_0}\right)^N, \tag{S3}$$

where $\tau_0 \equiv \sigma_0/\sqrt{3}$ and $\dot{\gamma}_0 \equiv \sqrt{3}\dot{\varepsilon}_0$.

In one-dimensional steady-flow of the fluid through a pipe, the velocity is only a function of the radial position r (Fig. S18) such that $\dot{\gamma} = -dv/dr$. The pressure drop Δp over the length h of the pipe follows from balancing the pressure drop with the shear stress at a radius r to give

$$\pi r^2 \Delta p = 2\pi r h \tau. \tag{S4}$$

Upon substituting for τ from (S3) into (S4) and using the definition of $\dot{\gamma}$ it follows that

$$-\frac{1}{\dot{\gamma}_0}\frac{dv}{dr} = \left(r\frac{\Delta p}{2h\tau_0}\right)^n, \tag{S5}$$

where $n \equiv 1/N$. Then integrate (S5) from $r = 0$ to $r = R$ with the sticking boundary condition $v = 0$ at $r = R$ to determine the maximum velocity $v_{\max}$ at $r = 0$ to be

$$\frac{v_{\max}}{\dot{\gamma}_0} = \frac{1}{n+1}\left(\frac{\Delta p}{2h\tau_0}\right)^n R^{(n+1)}, \tag{S6}$$

and $v(r)$ is

$$\frac{v}{\dot{\gamma}_0} = \frac{1}{n+1}\left(\frac{\Delta p}{2h\tau_0}\right)^n \left[R^{(n+1)} - r^{(n+1)}\right]. \tag{S7}$$

The flow rate $\dot{Q}$ through the pipe is

$$\dot{Q} = 2\pi \int_0^R r v dr = \pi R^2 \bar{v}, \tag{S8}$$

where $\bar{v}$ is the mean flow velocity through the pipe. From (S7) and (S8) it follows that

$$\bar{v} = \frac{3^{(n+1)/2}\dot{\varepsilon}_0}{n+3}\left(\frac{\Delta p}{2h\sigma_0}\right)^n R^{(n+1)}, \tag{S9}$$

where we have made use of $\tau_0 \equiv \sigma_0/\sqrt{3}$ and $\dot{\gamma}_0 \equiv \sqrt{3}\dot{\varepsilon}_0$.

S2.2 Non-linear creep version of the Kozeny-Carman analysis for flow through a porous medium

We use the analysis of Section S2.1 to derive a relation between the pressure drop Δp and mean flow velocity through a porous layer of thickness h comprising spherical particles of radius a and porosity ρ. The effective radius R of the equivalent circular pipe is assumed to be given by the Kozeny-Carman[4,5] approximation as

$$R \equiv \frac{\text{void volume}}{\text{wetted surface}}. \tag{S10}$$

Now consider a unit cell of volume $\mathcal{V}_0$ such that $1 - \rho \equiv (4/3)\pi a^3/\mathcal{V}_0$ where the wetted surface in volume $\mathcal{V}_0$ is $4\pi a^2$ and the void volume is $\rho\mathcal{V}_0$. Then,

$$R \equiv \frac{\rho a}{3(1-\rho)}. \tag{S11}$$

The far field fluid velocity v_∞ is related to the mean fluid velocity $\bar{v}$ through the porous layer as $v_\infty = \rho\bar{v}$. Upon substituting (S11) into (S9) it follows that

$$v_\infty = \frac{3^{\frac{n+1}{2}}\dot{\varepsilon}_0\rho}{n+3}\left(\frac{\Delta p}{2h\sigma_0}\right)^{n}\left[\frac{\rho a}{3(1-\rho)}\right]^{(n+1)}. \tag{S12}$$

Now consider the case of an applied Li$^+$ current i_s so that $v_\infty = i_s\Omega_{\mathrm{Li}}/F$ where F is the Faraday constant and Ω_{Li} the molar volume of Li. Then we set the stack pressure $p = \Delta p$ based on the assumption that fluid pressure drop over the thickness of the interface layer equals the stack pressure. The stack pressure p required to push the Li through the porous layer of thickness h to maintain a cell current i_s is

$$p = 2\sigma_0\left(\frac{h}{a}\right)\left(\frac{i_s\Omega_{\mathrm{Li}}}{F\dot{\varepsilon}_0 a}\right)^{\frac{1}{n}}\frac{(n+3)^{\frac{1}{n}}\left[3(1-\rho)^2\right]^{\frac{n+1}{2n}}}{\rho^{\frac{n+2}{n}}}. \tag{S13}$$

This relation can be interpreted as follows. For a given applied stack pressure p and stripping current i_s, the flow of Li through the interface layer is blocked when a layer of thickness h greater than that given by satisfaction of (S13). In this manner we can establish the capacity $C = C_{\mathrm{cr}}$ such that the flow is blocked.

Consider an electrode with a volume fraction f of spherical impurities of radius a. Upon stripping of Li from the electrode to reduce its height by H the volume of particles per unit area deposited on the interface is Hf. These particles form an interface layer of thickness h with a porosity ρ so that conservation of impurity particles implies $Hf = (1-\rho)h$. With $H = C\Omega_{\mathrm{Li}}/F$, where C is the stripped capacity, it follows that

$$C = \frac{hF}{\Omega_{\mathrm{Li}}}\frac{(1-\rho)}{f}. \tag{S14}$$

Now assume that the volume fraction of spherical impurities particles in the interface layer equals that of dense random packing density of mono-sized spherical particles, it follows [6,7] that $\rho = \rho_R = 0.36$. The critical value $C = C_{\mathrm{cr}}$ is obtained by substituting (S14) into (S13) to give

$$C_{\mathrm{cr}} = \frac{\rho_R^{\frac{n+2}{n}}(1-\rho_R)}{(n+3)^{\frac{1}{n}}\left[3(1-\rho_R)^2\right]^{\frac{n+1}{2n}}}\left(\frac{p}{2\sigma_0}\right)\left(\frac{F\dot{\varepsilon}_0 a}{i_s\Omega_{\mathrm{Li}}}\right)^{\frac{1}{n}}\frac{Fa}{f\Omega_{\mathrm{Li}}}. \tag{S15}$$

and the corresponding critical thickness h_{cr} of the interface layer is

$$\frac{h_{\mathrm{cr}}}{2a} = \frac{\rho_R^{\frac{n+2}{n}}}{2(n+3)^{1/n}\left[3(1-\rho_R)^2\right]^{(n+1)/(2n)}}\left(\frac{p}{2\sigma_0}\right)\left(\frac{F\dot{\varepsilon}_0 a}{i_s\Omega_{\mathrm{Li}}}\right)^{\frac{1}{n}}. \tag{S16}$$

This non-dimensional interface layer thickness $h_{\mathrm{cr}}/(2a)$ is plotted in Fig. S8 as a function of stack pressure p for realistic choices of impurity particle sizes $a = 100$ nm and $a = 1$ µm and currents $i_s = 1\ \mathrm{mAcm}^{-2}$ and $0.3\ \mathrm{mAcm}^{-2}$. The prediction shows that Li cannot flow through the impurity layer when it is more than ~ 2 particles thick. The Kozeny-Carman approximation used here requires $h_{\mathrm{cr}}/(2a) \gg 1$. The results in Fig. S8 suggest this limit of a porous interface layer that is many particles thick is not appropriate to understand the contact loss at the stripping interface.

S2.3 Interface layer that is one particle thick

The results in Section S2.2 suggest that the interface layer is ~1 particle thick for which the Kozeny-Carman analysis is not appropriate. Consequently, we proceed to consider the other extreme where the interface layer is one particle thick, i.e. thickness $h = 2a$.

Prior to developing the model, it is instructive to explain the physical picture. The Li/LLZO interface has an intrinsic resistance Z_0 associated with the barrier for Li-ions to cross the interface as analysed using Butler-Volmer kinetics. However, we measure the effective resistance over a large area of the interface and even in a pristine cell there are impurities on the interface (Fig. 2a). These impurities block the flow of Li-ions across the interface and reduce the effective area of the interface. Thus, the measured resistance Z of the pristine interface is $Z \geq Z_0$. Now consider stripping of the electrode, which results in deposition of impurities from within the electrode onto the interface. We shall discuss two cases: (i) the ideal case where the impurities are deposited in a spatially uniform manner and (ii) the more realistic case where impurities are deposited non-uniformly and might form patches.

First consider the case where impurity particles are deposited uniformly to form a monolayer. This layer is no longer characterised by a porosity ρ but rather by the centre-centre spacing 2ℓ of particles as sketched in Fig. 4b. *We again approximate the flow of the Li through this layer as flow through pipes but now take the pipes to be of length* $2a$ *and radius* $\ell - a$. The far field fluid velocity v_∞ is related to the mean fluid velocity $\bar{v}$ through each pipe as

$$\bar{v} = \frac{v_\infty}{1 - \left(\frac{a}{\ell}\right)^2}. \tag{S17}$$

Upon substituting (S17) for $\bar{v}$ in (S9) along with $R = \ell - a$, it follows (using $v_\infty = i_s \Omega_{\mathrm{Li}}/F$) that

$$\frac{\ell_{\mathrm{cr}}}{a} = \frac{1}{\sqrt{3}}\,(n+3)^{\frac{1}{n+1}} \left(\frac{4\sigma_0}{p}\right)^{\frac{n}{n+1}} \left[\frac{i_s \Omega_{\mathrm{Li}}}{a\dot{\varepsilon}_0 F} \frac{1}{1 - \left(\frac{a}{\ell_{\mathrm{cr}}}\right)^2}\right]^{\frac{1}{n+1}} + 1, \tag{S18}$$

where we label ℓ as ℓ_{cr} to recognise that when the particle spacing is ℓ_{cr}, flow through the porous layer under a stack pressure p is blocked. Given a volume fraction f of impurity particles in the electrode, this spacing is related to the stripped thickness H of the electrode via (1) as

$$H = a\left(\frac{a}{\ell_{\mathrm{cr}}}\right)^2 \frac{4}{3f}. \tag{S19}$$

This value of H is directly related to the critical capacity via $C_{\mathrm{cr}} = HF/\Omega_{\mathrm{Li}}$ yielding

$$\left(\frac{4Fa}{3C_{\mathrm{cr}}\Omega_{\mathrm{Li}} f}\right)^{1/2} = \frac{1}{\sqrt{3}}\,(n+3)^{\frac{1}{n+1}} \left(\frac{4\sigma_0}{p}\right)^{\frac{n}{n+1}} \left[\frac{i_s \Omega_{\mathrm{Li}}}{Fa\dot{\varepsilon}_0} \frac{1}{1 - \left(\frac{3C_{\mathrm{cr}}\Omega_{\mathrm{Li}} f}{4Fa}\right)}\right]^{\frac{1}{n+1}} + 1. \tag{S20}$$

Note that the interface resistance Z of the pristine interface (i.e. resistance prior to commencement of stripping) is absent from (S20) whereas our results (Figs. 3c and 3d) suggest that the critical capacity is sensitive to the interface resistance Z of the pristine cell. We now extend the analysis to understand the dependence of C_{cr} on Z.

The micrographs in Fig. 2a show that the as-manufactured pristine interface has a scattering of impurity particles that shield the interface from Li transport. These particles are insulating in the sense that they do not conduct Li and therefore reduce the effective area of the interface such that a higher concentration of particles implies a higher average interface resistance of the pristine interface. Let Z_0 denote the interface resistance in the absence of any impurity particles. The presence of impurity particles of radius a_0 spaced a distance $2\ell_0$ apart implies that a fraction $(a_0/\ell_0)^2$ of the interface no longer conducts Li. The resistance Z of the pristine interface (prior to stripping) is

$$Z = \frac{Z_0}{1 - \left(\frac{a_0}{\ell_0}\right)^2}. \tag{S21}$$

The presence of these pre-existing particles implies that we need to strip a smaller height compared to (S19) as the particle spacing on the interface only needs to reduce from ℓ_0 to ℓ_{cr} rather than from ∞ to ℓ_{cr}.

We estimate this reduced stripping height in an approximate way as follows. Assume an interface with no initial impurity particles. Stripping a height H_0 of the electrode with a volume fraction f of particles of radius a will result in a spacing ℓ_0 of particles deposited on the electrode. Then, using an analysis analogous to (S19) we obtain

$$H_0 = a\left(\frac{a}{\ell_0}\right)^2 \frac{4}{3f} = a\left(\frac{a_0}{\ell_0}\right)^2 \left(\frac{a}{a_0}\right)^2 \frac{4}{3f}. \tag{S22}$$

Substituting for a_0/ℓ_0 from (S21), we obtain

$$H_0 = a\left(1 - \frac{Z}{Z_0}\right)\left(\frac{a}{a_0}\right)^2 \frac{4}{3f}. \tag{S23}$$

The critical stripping height (S19) is then assumed to be reduced by H_0 as the stripping only needs to decrease the spacing from ℓ_0 to ℓ_{cr} to block the flow of Li, i.e. the critical stripping height $H_{\mathrm{cr}} = H - H_0$, where H is given by (S19). Thus,

$$H_{\mathrm{cr}} = a\frac{4}{3f}\left[\left(\frac{a}{\ell_{\mathrm{cr}}}\right)^2 - \left(1 - \frac{Z}{Z_0}\right)\left(\frac{a}{a_0}\right)^2\right]. \tag{S24}$$

and C_{cr} is given by

$$C_{\mathrm{cr}} = \frac{4aF}{3f\Omega_{\mathrm{Li}}}\left[\left(\frac{a}{\ell_{\mathrm{cr}}}\right)^2 - \left(1 - \frac{Z}{Z_0}\right)\left(\frac{a}{a_0}\right)^2\right], \tag{S25}$$

with ℓ_{cr} given by the solution to (S18).

This model requires 4 key parameters (Z_0, a_0, a, f) which are estimated as follows. The Li electrodes have a high purity with the manufacturer specifying ~ 99.9% Li. We thus set $f = 0.1\%$. The particle sizes a and a_0 are not known but our micrographs (Figs. 2a and 2b) suggest submicron sizes and thus we chose $a = 130$ nm and $a_0 = 200$ nm. Finally, we set $Z_0 = 1\ \Omega\mathrm{cm}^{-2}$ which equals the lowest value of Z that we measured over the 50 specimens we manufactured as part of this study.

The prediction (S25) only gives the critical capacity at which the flow of Li is completely blocked but not the temporal evolution of cell voltage (Fig. 1c). We now extend this model to give the temporal evolution of cell voltage in this limit of spatially uniform distribution of impurity particles on the interface. In this limit, the fraction of the active area at any instant is $[1 - (a/\ell)^2]$ and prior to the complete block of Li-ion flux the cell voltage is related to capacity C via Eq. (2). This equation is valid for $C < C_{\mathrm{cr}}$ and the voltage-capacity relation is then given by the piecewise function

$$V_{\text{cell}} = i_s \left[Z \left\{ \frac{1}{\left(1 - \frac{3fC\Omega_{\text{Li}}}{4Fa}\right)} + 1 \right\} + \frac{L_E}{\kappa} \right] \qquad C < C_{\text{cr}}, \qquad \text{and} \tag{S26}$$

$V_{\text{cell}} = \infty$, for $C \geq C_{\text{cr}}$. Comparisons between this prediction and measurements from Fig. 1c are included in Fig. S10 (with cell parameters $= 9\ \Omega\text{cm}^2$, $L_E = 1$ mm and $\kappa = 0.47\ \text{mS cm}^{-1}$). We observe that while the capacity C_{cr} at which the voltage increases sharply is predicted with good fidelity, the model does not predict the more gradual increase in voltage immediately prior to the critical condition.

This discrepancy is associated with the fact that in reality the deposition of impurities is spatially non-uniform. As argued in the main text, for a given stack pressure p, (S18) gives the critical inter-particle spacing ℓ_{cr} below which Li flow to the interface is blocked. Now consider a non-uniform distribution of impurities particles on the interface (Fig. 5b). Parts of the interface where $\ell \leq \ell_{\text{cr}}$ become inactive and Li-ion flux is restricted to regions of the interface where $\ell > \ell_{\text{cr}}$, i.e. the effective area of the interface is less than the electrode area. Now recall that the imposed voltage controls the Li-ion flux across the active parts of the interface via the usual Butler-Volmer kinetics. As deposition continues, the parts of the interface that are insulating increase. Under galvanotactic loading this implies that the cell voltage needs to increase to maintain the total current as the active area of the interface decreases. This gives rise to the more gradual increase in cell voltage immediately prior to attainment of the critical capacity observed in the measurements (Fig. 1c and S4).

S2.4 Time for Li to creep through the one particle thick interface layer

In the strip-rest experiments (Fig. 5), the resistance recovers in the rest period as Li creep through the gaps between the impurity particles and re-establishes contact with the LLZO interface. We wish to estimate the time for this recovery period. Recall that we are approximating the flow of the Li through this one particle thick layer as flow through a pipe of radius $R = \ell - a$. The mean flow velocity is given by (S9) as

$$\bar{v} = \frac{3^{(n+1)/2}\dot{\varepsilon}_0}{n+3} \left(\frac{p}{2s\sigma_0}\right)^n (\ell - a)^{(n+1)} \tag{S27}$$

where we replace Δp by p based on the assumption that the pressure drops to zero over the distance s that the Li has flowed through the pipe of length $2a$. Then,

$$\frac{ds}{dt} = \bar{v}\,, \tag{S28}$$

and contact is re-established at time $t = t_R$ when $s = 2a$. Integrating (S28) gives t_R as

$$t_R = \frac{1}{\dot{\varepsilon}_0} \left(\frac{1}{3^{(n+1)/2}} \frac{n+3}{n+1} \right) \left(\frac{2\sigma_0}{p}\right)^n \left(\frac{2}{\ell/a - 1}\right)^{(n+1)}. \tag{S29}$$

Predictions of t_R as a function of non-dimensional impurity particle spacing ℓ/a are included in Fig. S11 for three choices of the stack pressure p. At $p = 10$ MPa, a recovery time $t_R \sim 1$ hr is predicted for $\ell/a \sim 1.19$. With particles assumed to be $a = 130$ nm (consistent with the size used for the predictions in Figs. 3c and 3d), we therefore infer a spacing $2\ell \sim 310$ nm for a recovery time of 1 hr. This spacing is broadly consistent with the observations of the stripped interface in Fig. 2b.

S2.5 Time for recovery of resistance during a rest period

The measurements (Figs. 6 and 7) show an increase in the resistance during stripping and a gradual recovery of the resistance during rest. The analysis of section S2.4 can be used to estimate this recovery time during the rest periods. The increase in resistance is governed by patches on the interface where the particle spacing $s < s_{\mathrm{cr}} \equiv \ell_{\mathrm{cr}} - a$. In these patches, the imposed pressure cannot force the Li through the gaps between the particles at a rate sufficient to keep up with the imposed stripping current and hence contact between the Li and the electrolyte is lost in those regions. Recovery of the resistance occurs when contact is re-established in these regions during rest via creep of Li under the continued imposed stack pressure.

We thus consider patches with a spacing $s = \alpha s_{\mathrm{cr}}$ where $0 < \alpha \leq 1$, i.e. regions where contact of Li with the electrolyte was lost. With s_{cr} given by (S18), the recovery time follows from (S29) as

$$t_R = \frac{1}{\dot{\varepsilon}_0}\left(\frac{1}{3^{(n+1)/2}}\frac{n+3}{n+1}\right)\left(\frac{2\sigma_0}{p}\right)^n\left(\frac{2a}{\alpha s_{\mathrm{cr}}}\right)^{(n+1)}, \tag{S30}$$

with

$$\frac{s_{\mathrm{cr}}}{a} = \frac{1}{\sqrt{3}}\,(n+3)^{\frac{1}{n+1}}\left(\frac{4\sigma_0}{p}\right)^{\frac{n}{n+1}}\left[\frac{i_s\Omega_{\mathrm{Li}}}{a\dot{\varepsilon}_0 F}\frac{1}{1-\dfrac{1}{(1+s_{\mathrm{cr}}/a)^2}}\right]^{\frac{1}{n+1}}, \tag{S31}$$

It is worth considering the limit $s_{\mathrm{cr}}/a \gg 1$ such that (S31) reduces to

$$\frac{s_{\mathrm{cr}}}{a} \approx \frac{1}{\sqrt{3}}\,(n+3)^{\frac{1}{n+1}}\left(\frac{4\sigma_0}{p}\right)^{\frac{n}{n+1}}\left[\frac{i_s\Omega_{\mathrm{Li}}}{a\dot{\varepsilon}_0 F}\right]^{\frac{1}{n+1}}, \tag{S32}$$

and substituting (S32) into (S30) gives

$$t_R \approx \frac{2}{\dot{\varepsilon}_0}\left(\frac{1}{\alpha}\right)^{(n+1)}\frac{a\dot{\varepsilon}_0 F}{i_s\Omega_{\mathrm{Li}}}, \tag{S33}$$

such that t_R is independent of the stack pressure p. This independence arises from the two opposing effects of pressure discussed in the main text. The predictions in Fig. 6d use the full equations without making the approximation that $s_{\mathrm{cr}}/a \gg 1$ and gives a mild dependence of t_R on stack pressure.

S3: Calculation of the interface resistance Z in the Li/LLZO/Li cells with different electrode areas

By fitting the equivalent circuit (Fig. S15) to the measured PEIS spectrum of each cell, we extracted the combined interface resistance $R_{\mathrm{interface}}$ (Ω) of both interfaces and the total cell resistance $R \equiv R_{\mathrm{interface}} + R_B + R_{GB}$. This total resistance is plotted in Figs. 5b and 5c. Since the two electrodes of a cell are assembled in similar fashion, the effective interface resistance, Z (Ωcm^2) of both interfaces can be assumed to be equal. Total interface resistance $R_{\mathrm{interface}}$ in terms of Z is

$$R_{\mathrm{interface}} = \frac{Z}{A_1} + \frac{Z}{A_2}, \tag{S30}$$

where A_1 and A_2 are the areas of the two electrodes estimated from optical images. Then given $R_{\mathrm{interface}}$ it follows that

$$Z = R_{\mathrm{interface}} \frac{A_1 \, A_2}{A_1 + A_2}. \tag{S31}$$

These are the values of interface resistance that we cite in the main text.

Supplementary Figures

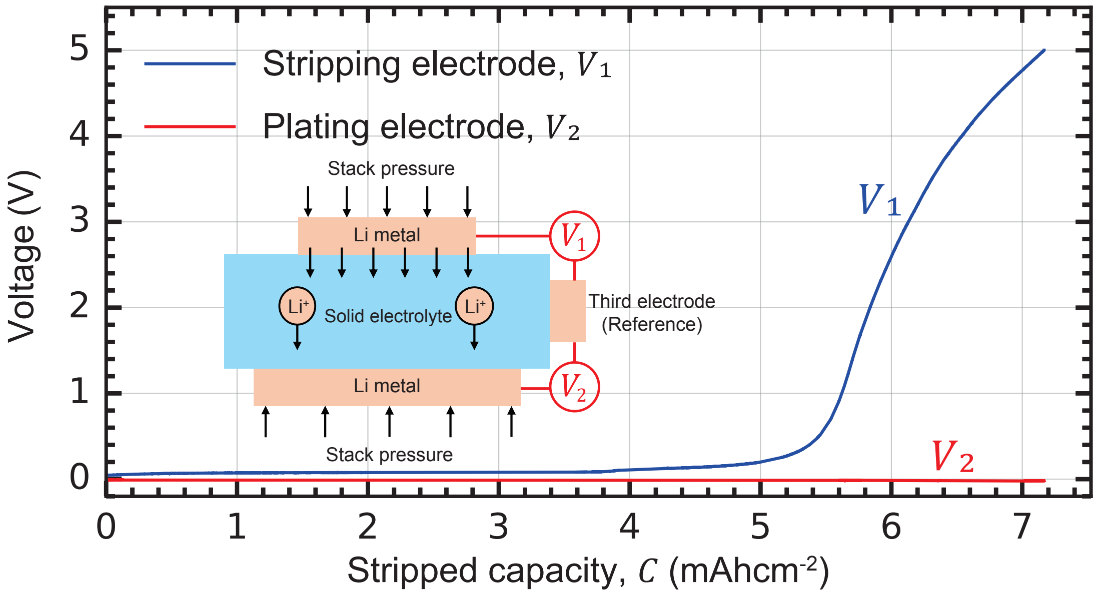

Figure S1: Three electrode cell test under a stack pressure $p = 10$ MPa and stripping current density $i_s = 0.3$ mAcm^{-2} (interface resistance $Z \approx 14$ Ωcm^2). The voltage drop across the plating and stripping interfaces is plotted as function of the stripped capacity $C = i_s t$, where time $t = 0$ at the start of the galvanostatic loading. The assembly of the 3-electrode cell and associated measurement of the stripping and plating electrode voltages is indicated in the inset. Briefly, the third electrode was assembled by physically attaching a small piece of Li metal on the hand polished curved surface of the cylindrical pellet after the cell was fabricated (*Methods*). Based on these measurements, the rise in cell voltage (Fig. 1c) can be ascribed exclusively to the stripping interface as the voltage across the plating interface remains unchanged.

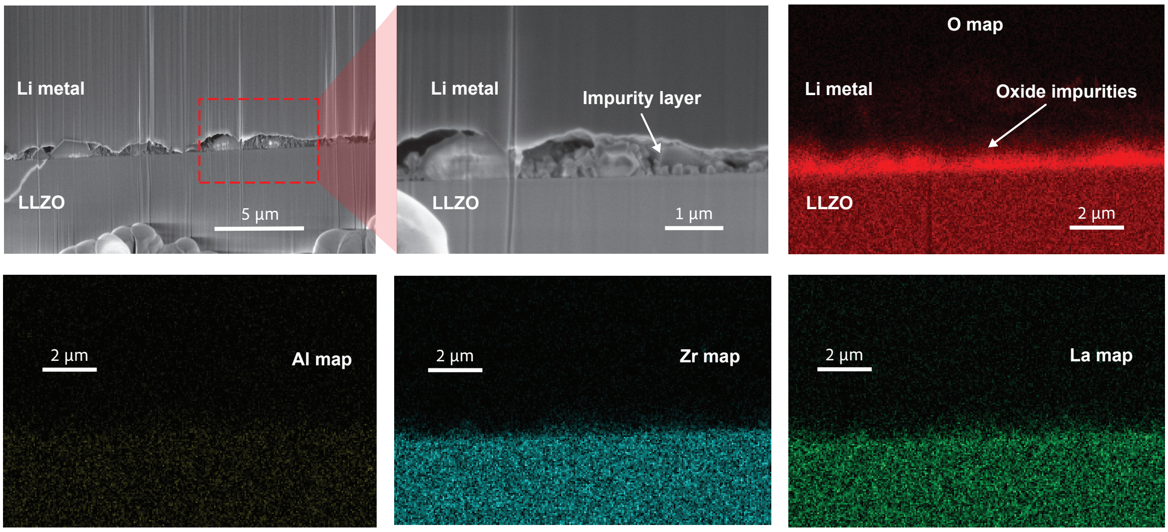

Figure S2: Cryo-PFIB-SEM images of the interface after stripping at $i_s = 1$ mAcm^{-2} with a stack pressure 10 MPa, the images are taken after the cell voltage has risen to 5 V (same as shown in Fig. 2b). The images are shown at two levels of magnification (region of higher magnification indicated by the red dashed box). EDS maps to indicate the distribution of Oxygen, Aluminium, Lanthanum and Zirconium are included in this higher magnificent region. The impurity layer only shows a higher oxygen signal suggesting the impurities are not formed due to milling induced redeposition.

a) Stripped at 1 $mAcm^{-2}$ upto 2V

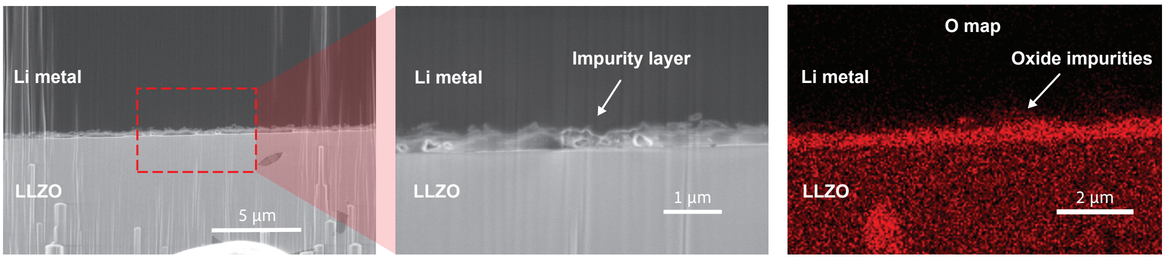

b) Stripped at 0.3 $mAcm^{-2}$ upto 2V

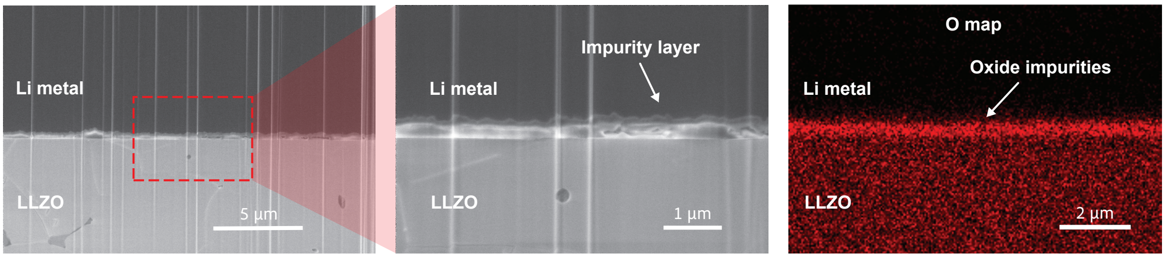

Figure S3: Cryo-PFIB-SEM images of the interface after stripping at i_s = (a) $1\ \mathrm{mAcm}^{-2}$ and (b) $0.3\ \mathrm{mAcm}^{-2}$ with a stack pressure 10 MPa. The images are taken after the cell voltage has risen to 2 V and both cells had an initial interface resistance $Z \approx 5\ \Omega\mathrm{cm}^2$ (i.e., prior to galvanostatic testing). The images are shown at two levels of magnification (higher magnification indicated by the red dashed boxes) and include Oxygen EDS maps to show the high oxygen content in the layer of deposited impurities.

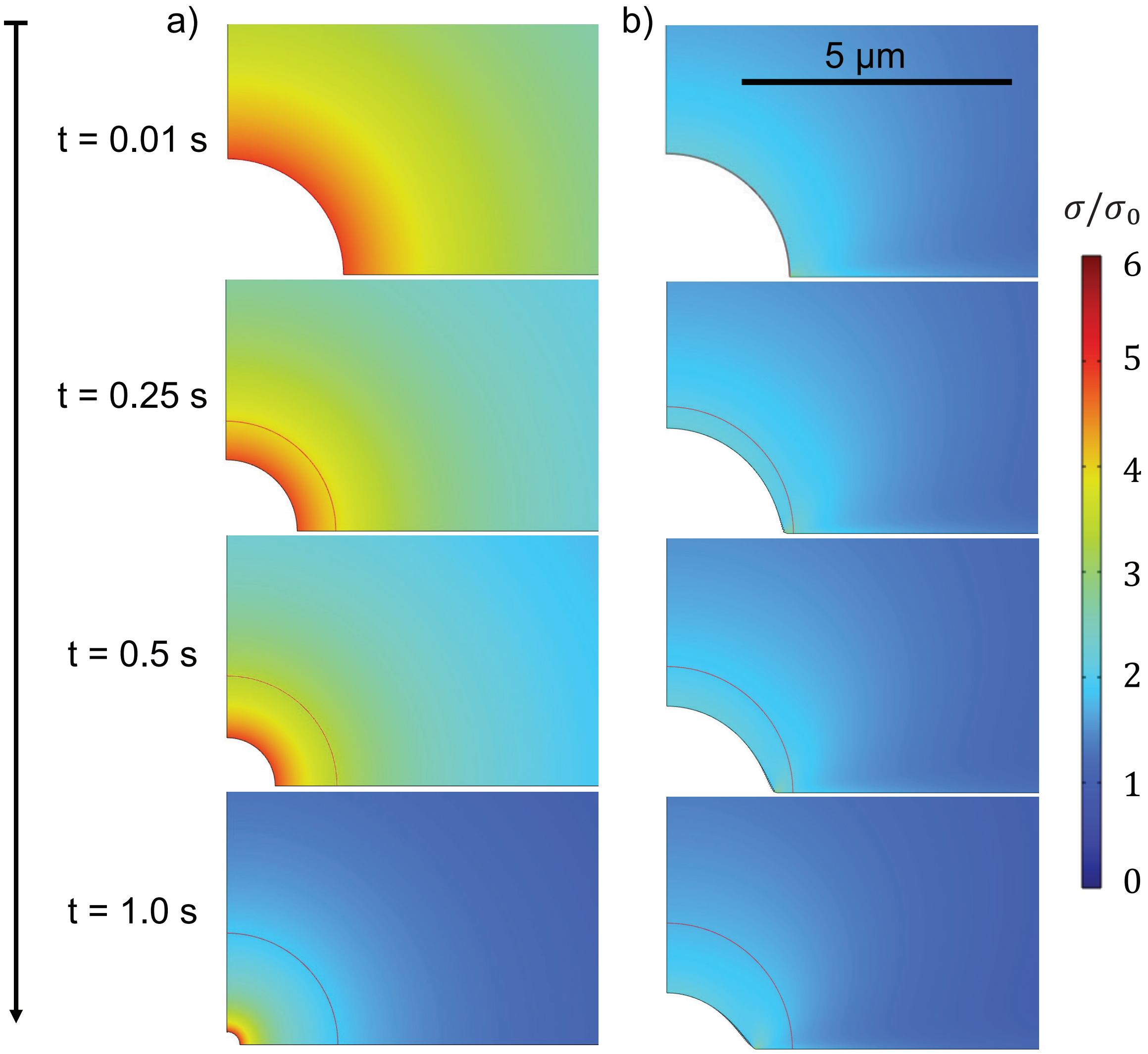

Figure S4: Predictions of the collapse of a $a_{\rm v} = 25$ μm hemispherical void under a 10 MPa stack pressure. Results are shown at selected times with time $t = 0$ corresponding to the instant the pressure was imposed. The predictions show the temporal evolution of the void shape with contours of the normalised von-Mises stress in the Li also included. Results are shown for (a) frictionless and (b) sticking boundary conditions of the Li along the electrode/electrolyte interface.

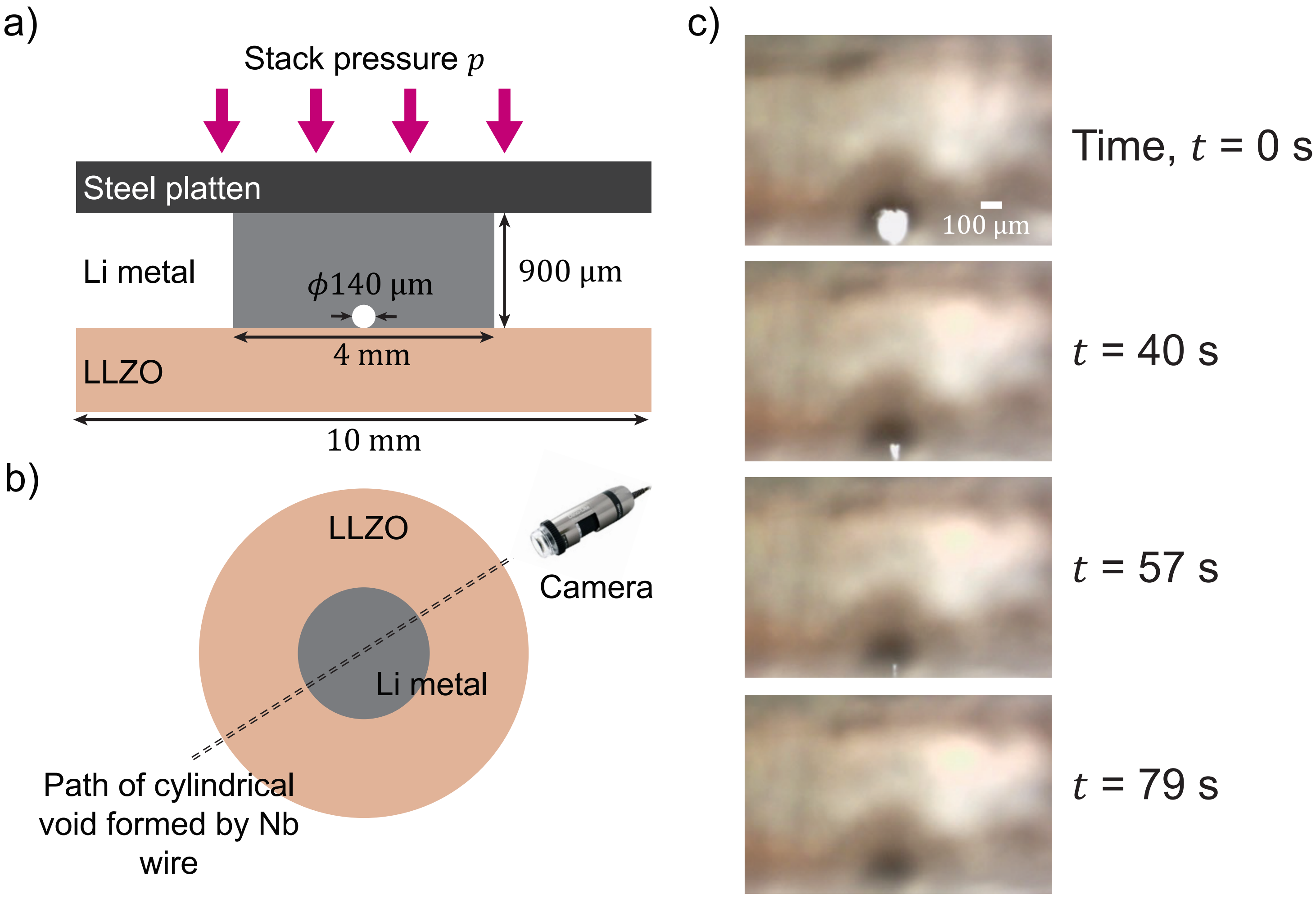

Figure S5: Observations of the collapse of a void on the interface between an Li film and LLZO. The measurements were carried out using the protocol developed in Roach et al.[8] (a) Sketch of measurement setup with a Li film of diameter $\sim$ 4 mm and thickness $\sim$ 900 μm bonded to LLZO. A cylindrical void of diameter $\sim$ 140 μm was created by pressing Li metal over a Nb wire of diameter 200 μm . The wire was later withdrawn to leave the void. (b) Photograph of the plan view of the Li film showing the path of the cylindrical void. (c) Side (elevation) view observations of the collapse of the void under an imposed stack pressure $p = 1.4$ MPa. Time $t = 0$ corresponding to the instant the pressure was imposed the void completely disappears shortly after $t = 79$ s.

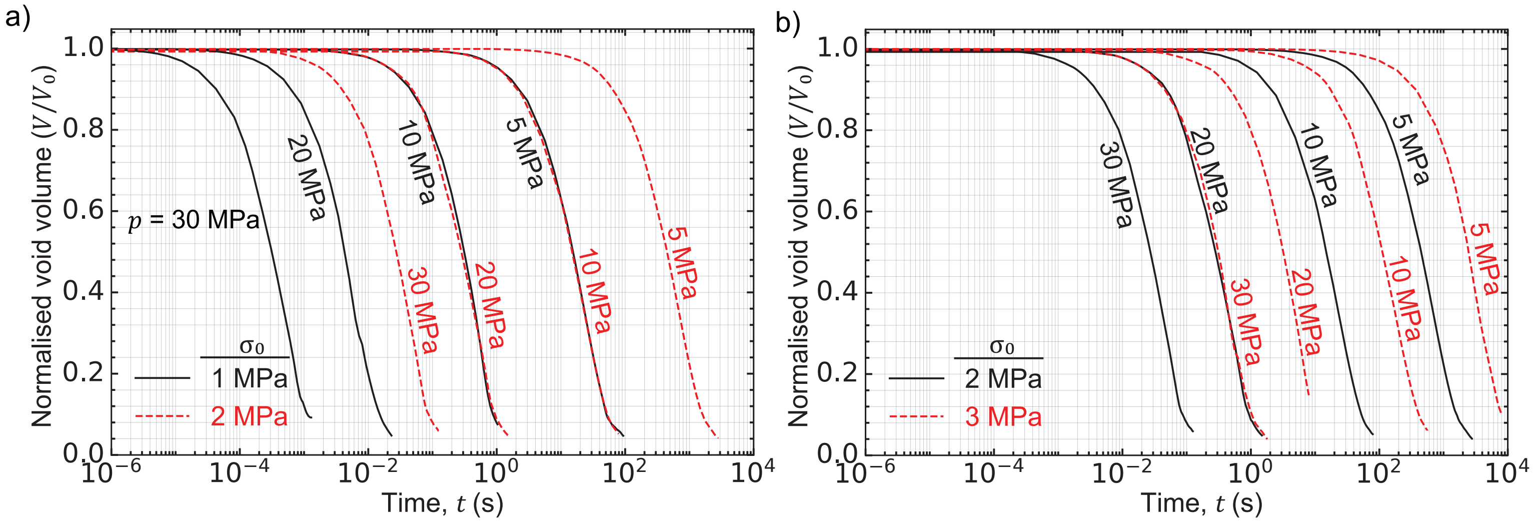

Figure S6: Additional calculations to supplement those in Fig. 3b to illustrate the effect of the Li creep strength σ_0 on the time for voids to collapse. Calculations are reported for σ_0 in the range 1 MPa $\leq \sigma_0 \leq$ 3 MPa which correspond to measured strengths in the range > 100 µm to ~15 µm[9]. All other material constants are the standard values used in the calculations in Fig. 3b and here predictions are only reported for the frictionless sliding between the Li and the rigid interface. Comparison between predictions of the temporal evolution (time $t = 0$ at the instant of the application of pressure) of the normalised void volume V/V_0, where V_0 is the initial void volume for selected imposed stack pressures p for creep strengths (a) $\sigma_0 = 1$ MPa and 2 MPa and (b) $\sigma_0 = 2$ MPa and 3 MPa.

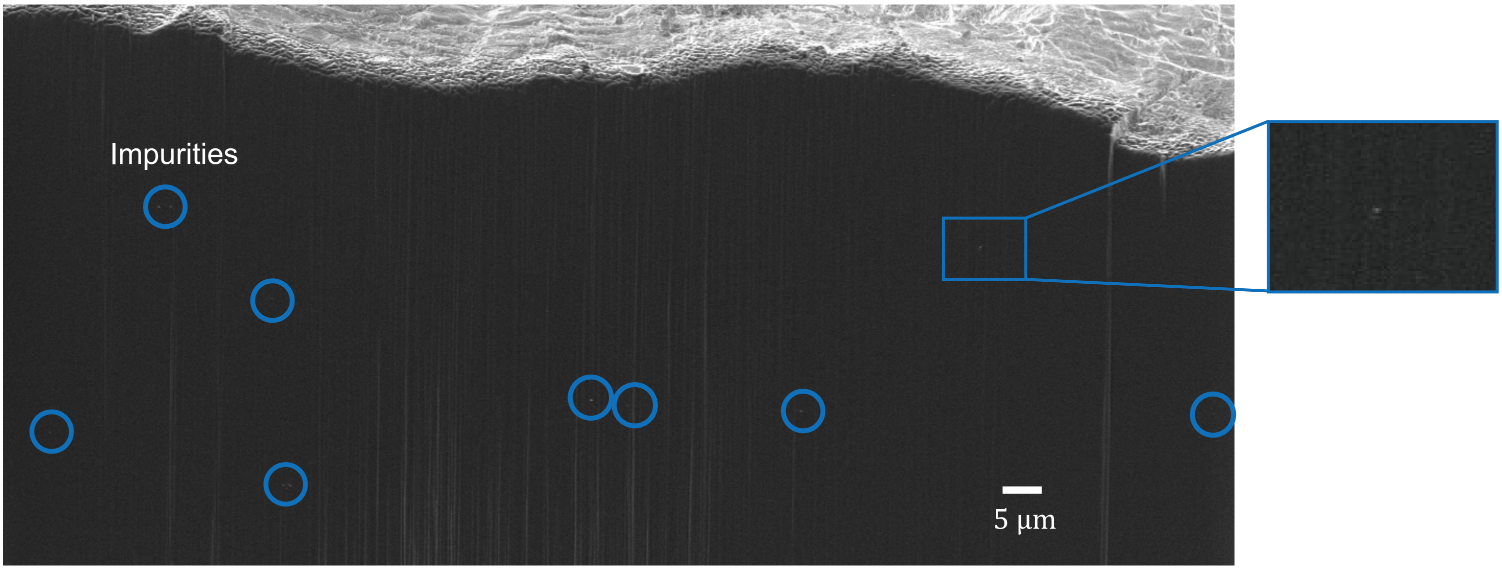

Figure S7: Cryo-PFIB-SEM images of the bulk pristine Li electrode that shows a dilute dispersion of impurity particles.

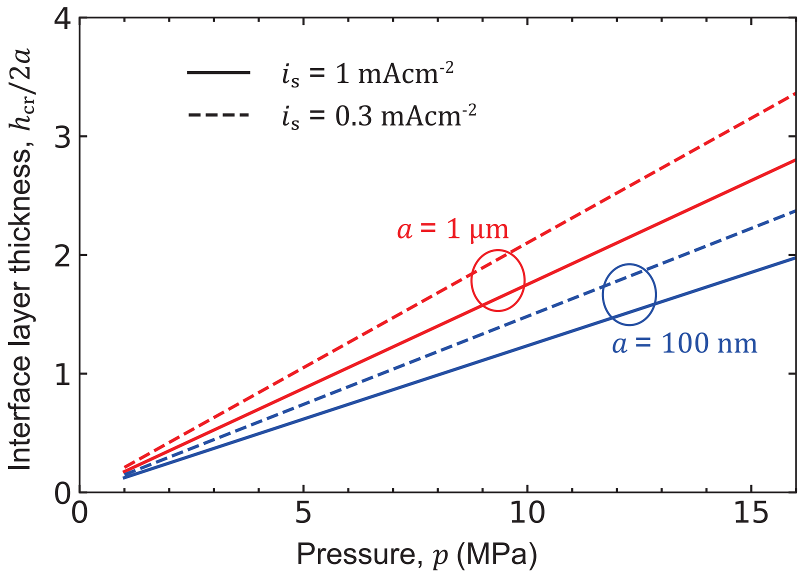

Figure S8: Non-linear Kozeny-Carman predictions (S16) of the non-dimensional critical thickness $h_{cr}/(2a)$ at which flow of Li through the porous impurity layer on the interface is blocked. Results are shown for impurity particles of size $a = 100$ nm and 1 µm and currents $i_s = 1$ mAcm^{-2} and 0.3 mAcm^{-2}.

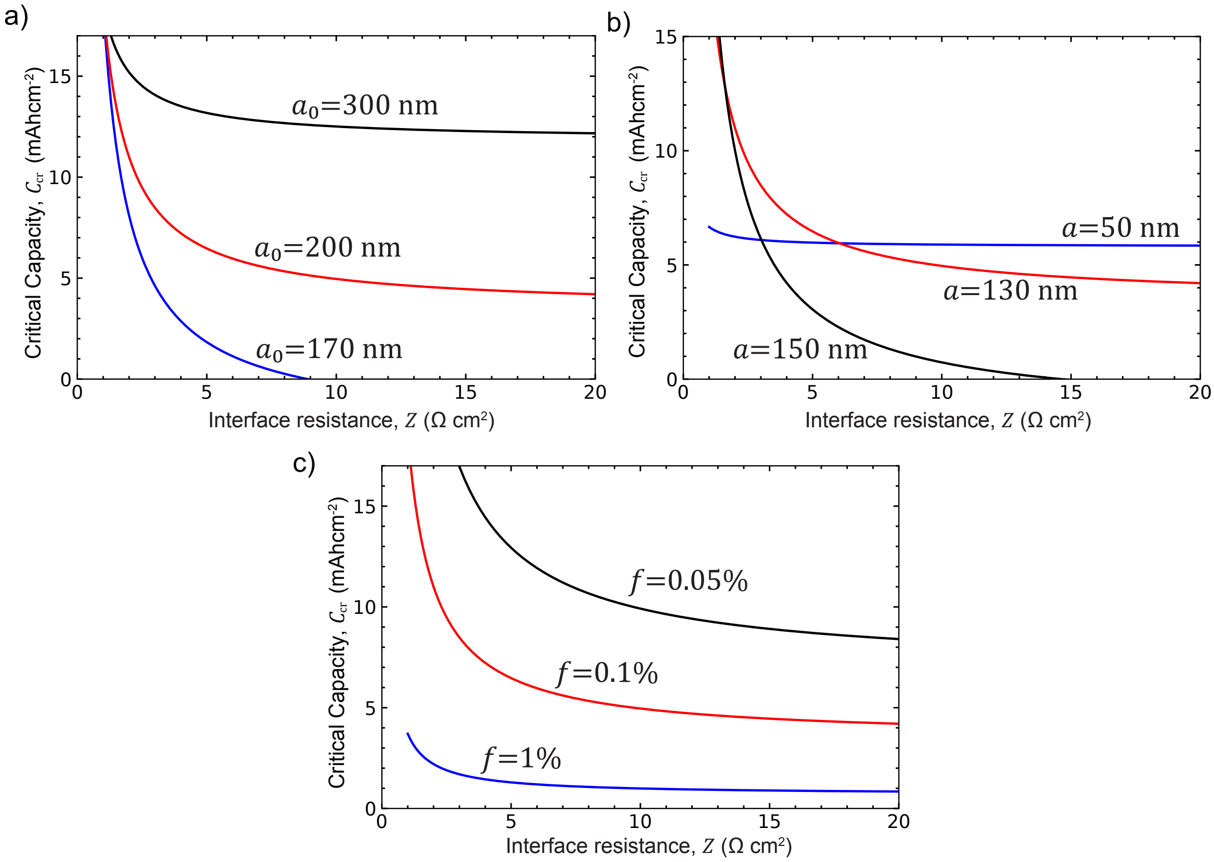

Figure S9: Sensitivity of critical capacity C_{cr} predictions (S25) to the size of impurity particles a_0 on the pristine interface, size of a of impurity particles deposited on the interface during stripping, and impurity volume fraction f in the bulk Li. Predicted capacities are shown for (a) 3 choices of a_0 with fixed $a = 100$ nm and $f = 0.1\%$, (b) 3 choices of a with fixed $a_0 = 200$ nm and $f = 0.1\%$, and (c) 3 choices of f with $a_0 = 200$ nm and $a = 100$ nm. All results are for a stack pressure p of 10 MPa and a stripping current of 1 mAcm^{-2}.

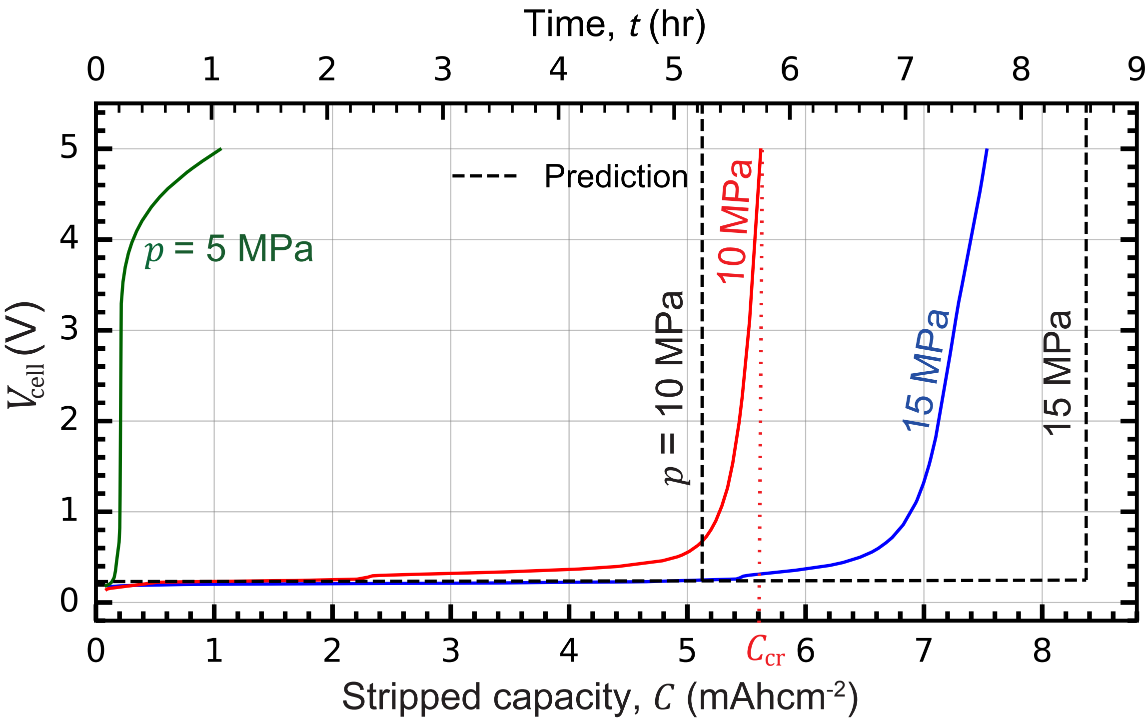

Figure S10: Comparison between the measurements and predictions of the cell voltage V_{cell} as a function of stripped capacity C. The measurements are those in Fig. 1c and the predictions are for the model with a monolayer of uniformly distributed impurity particles; Eq. (S26).

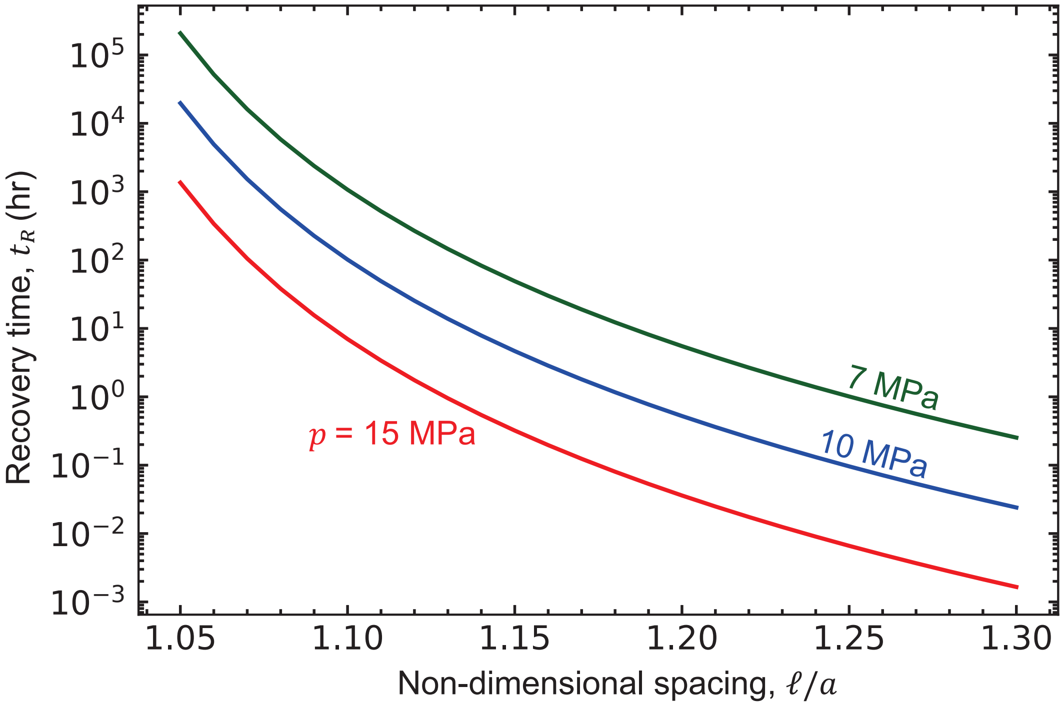

Figure S11: Predictions of the recovery time t_R as a function of non-dimensional spacing ℓ/a for a single layer of impurity particles on the interface. Results are shown for selected stack pressures p.

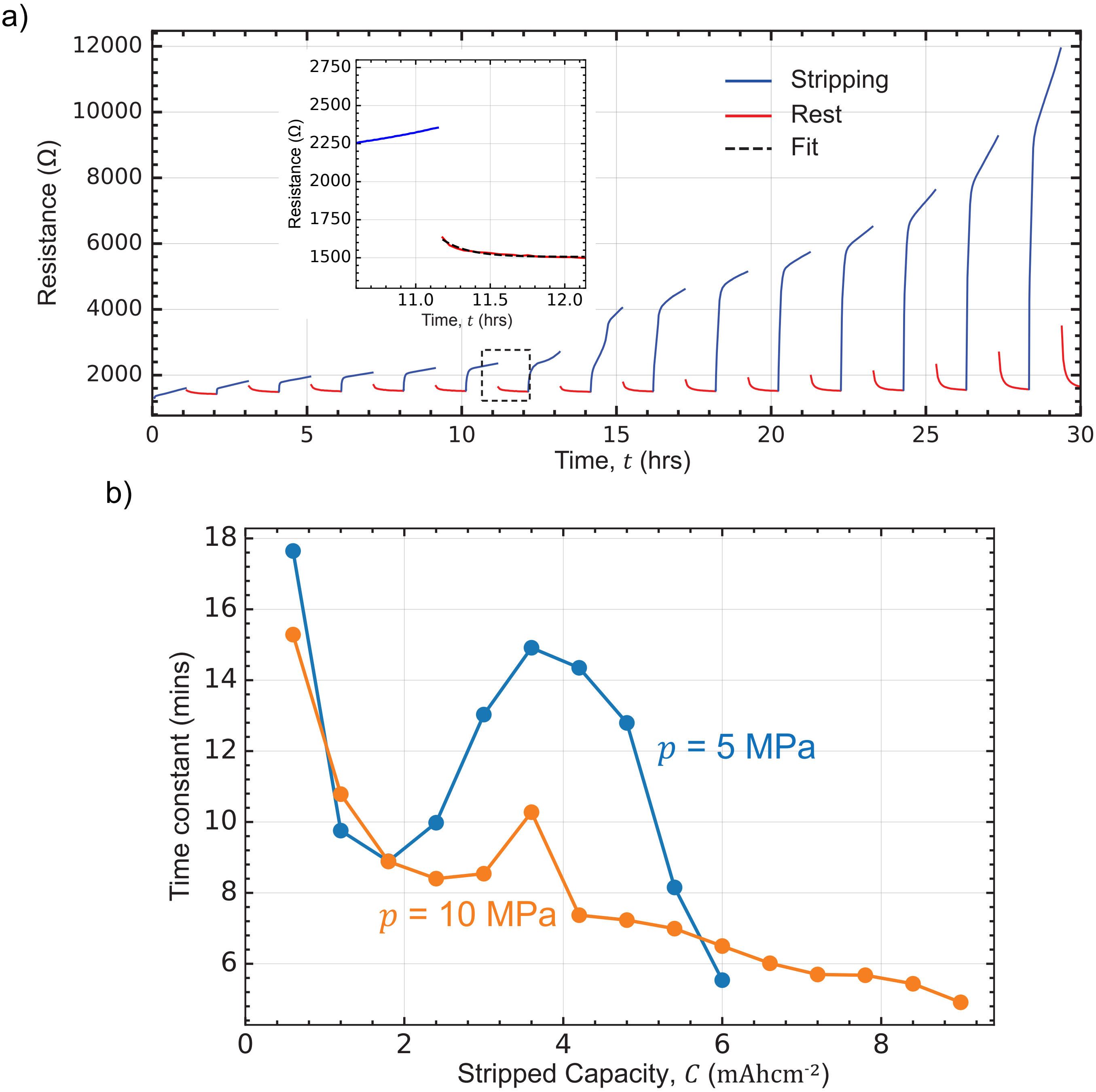

Figure S12: (a) The strip-rest experiments of Fig. 6b showing the recovery of the resistance during the rest periods. The inset shows the fitting of an exponential function to the resistance during rest to extract the time constant τ over which the resistance recovers. (b) The extracted recovery constants τ as a function of the stripped capacity C prior to each rest period. Data is shown for the experiments of Fig. 6 with a stripping current $i_s = 0.6$ mAcm^{-2} and stack pressures $p = 5$ MPa and 10 MPa.

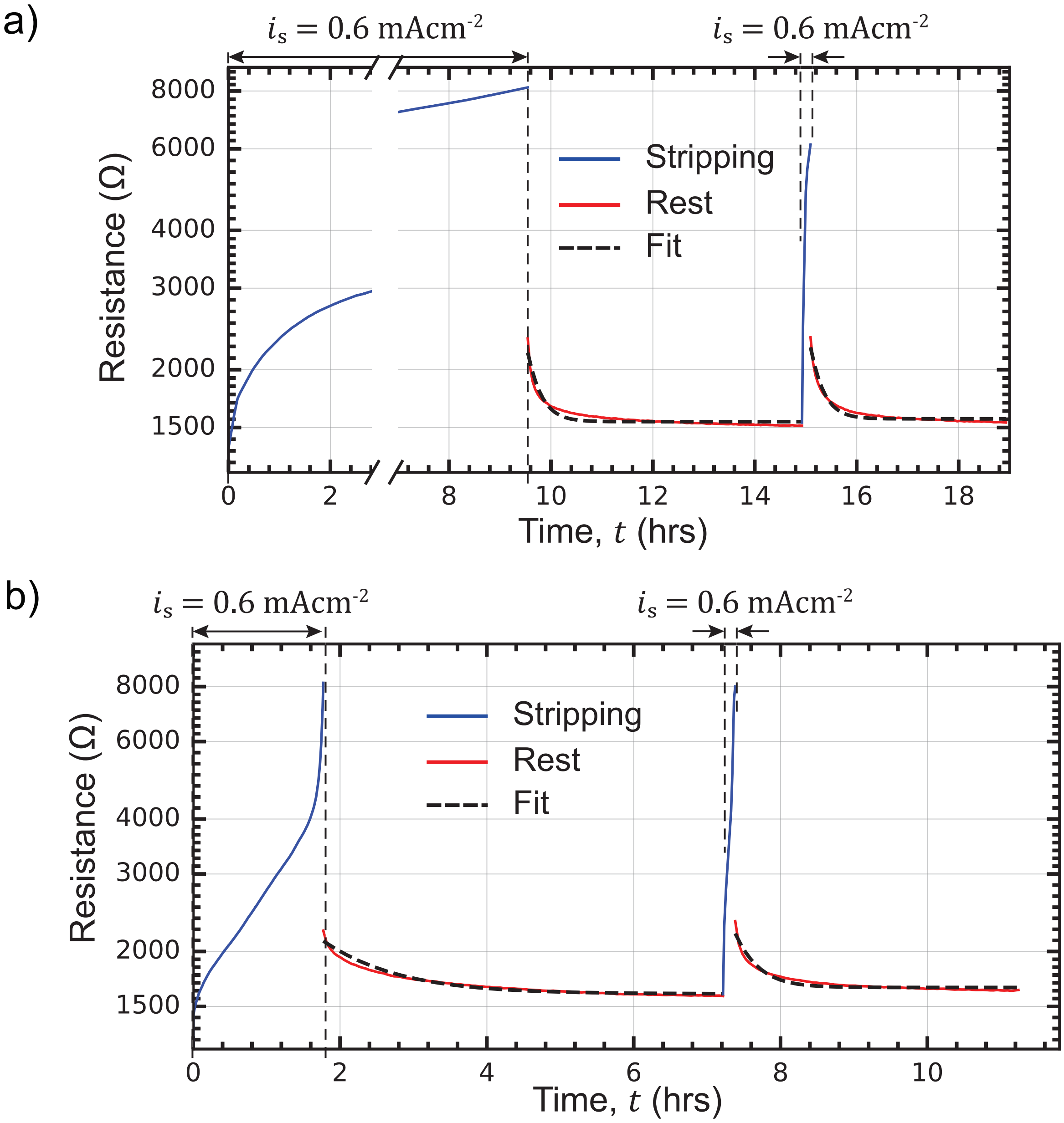

Figure S13: Additional strip-rest experiments with a protocol akin to Fig. 7a. A stripping current $i_s = 0.6\ \mathrm{mAcm}^{-2}$ is applied for to a capacity $\sim 6\ \mathrm{mAhcm}^{-2}$ followed by a rest of 4 hrs under a stack pressure (a) $p = 10$ MPa and to a capacity of $\sim 1.2\ \mathrm{mAhcm}^{-2}$ followed by a rest of 4 hrs under (b) 5 MPa, so that in both samples rise in interfacial resistance was of similar values. The exponential fit to the recovery of the resistance is shown in both cases and the recovery constants extracted from these measurements are included in Fig. 6d.

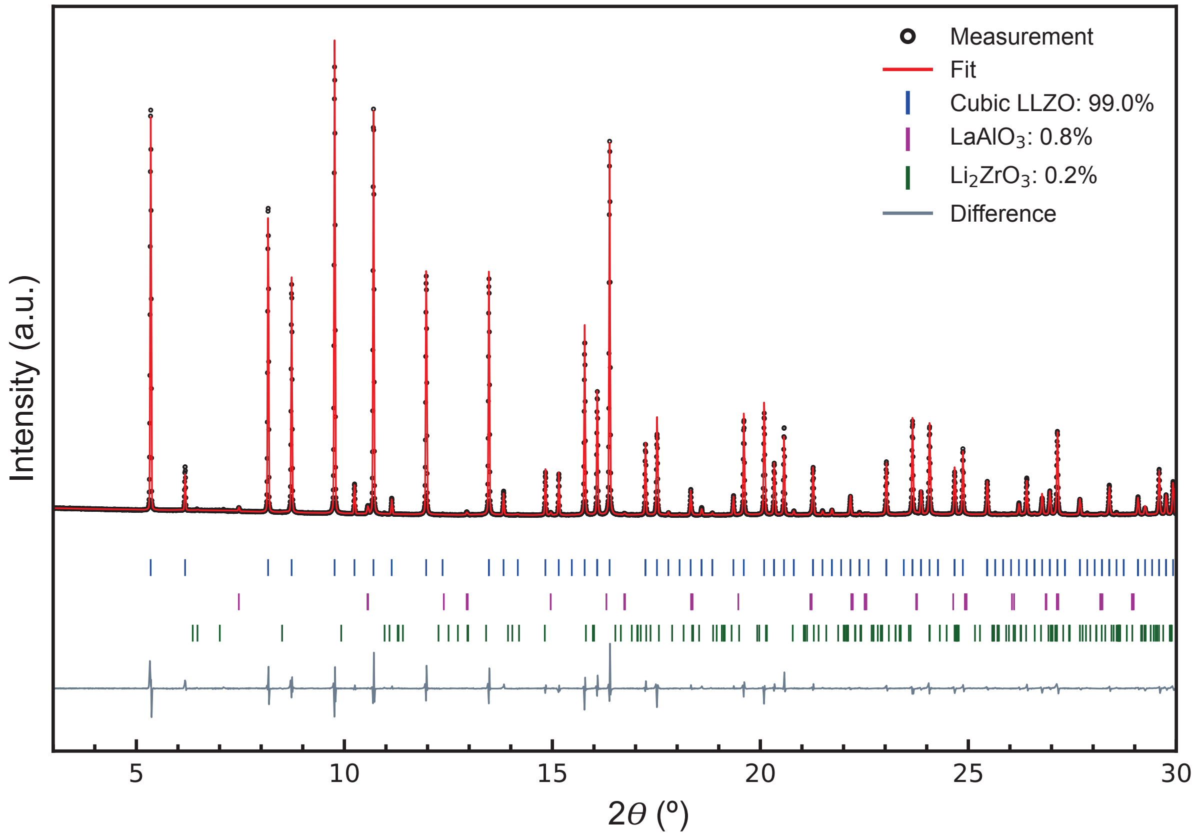

Figure S14: Synchrotron X-ray diffraction spectrum of hot-pressed Al-LLZO pellet (λ = 0.493 Å) along with its Rietveld refinement to extract phase fraction of Al-LLZO and the minor side-products. The difference profile indicates the fit quality (Bragg R-factor = 3.16).

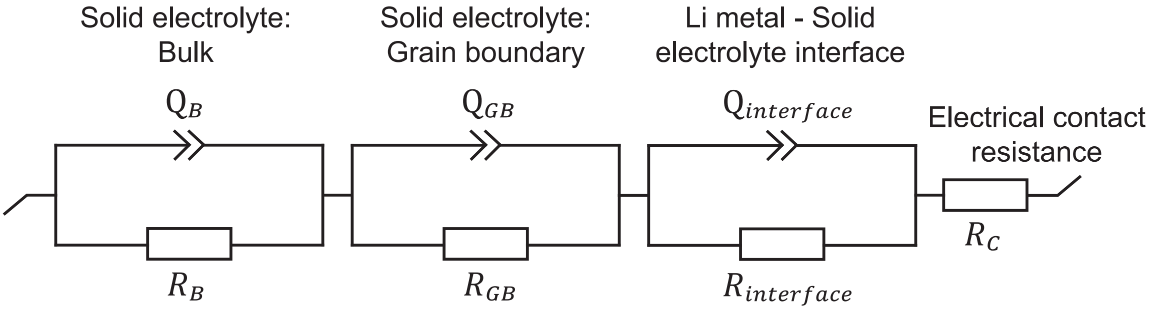

Figure S15: Equivalent circuit used to fit the impedance data of Li-LLZO-Li cells. The symbols, R_i represents resistances while Q_i represents constant phase elements (non-ideal capacitor).

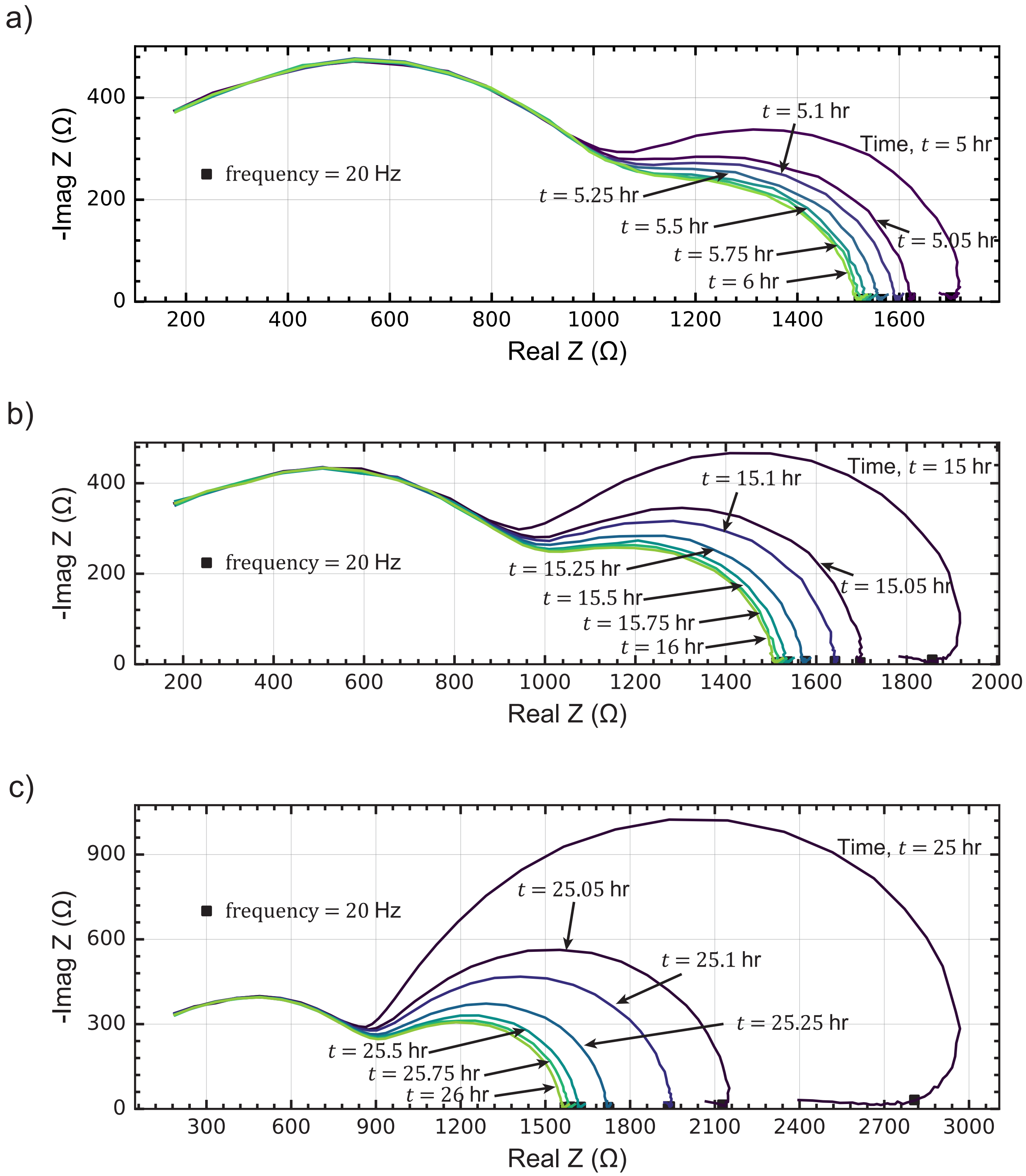

Figure S16: The evolution of PEIS spectra during the rest periods. The spectra are shown for three selected rest periods for the data in Fig. 6a. (a) 5 hr $\leq t \leq$ 6 hr; (b) 15 hr $\leq t \leq$ 16 hr and (c) 25 hr $\leq t \leq$ 26 hr. In each case selected spectra are shown with the times labelled and the real part of impedance spectrum at 20 Hz used as an approximation for the total cell resistance R is marked in each case.

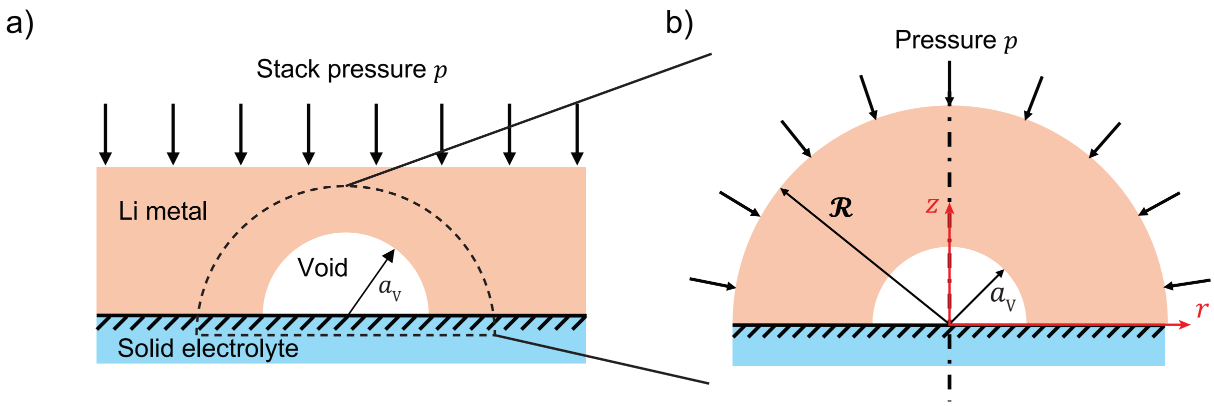

Figure S17: (a) Sketch of a hemispherical void in a large Li electrode subjected to a stack pressure (repeated from Fig. 3a). (b) Sketch of the boundary value problem analysed to investigate the collapse of the voids under stack pressure.

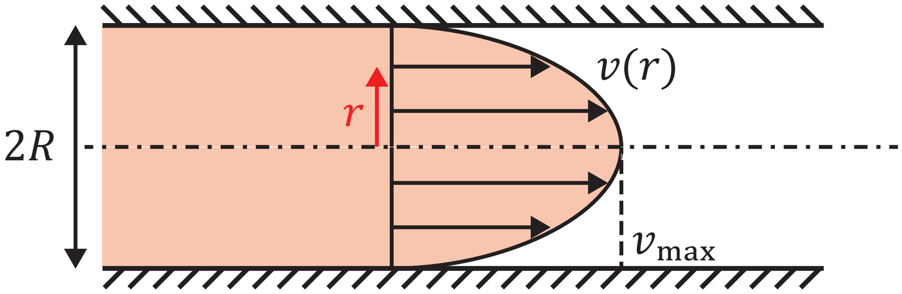

Figure S18: Sketch of the steady-state flow velocity field for flow of a fluid through a circular pipe of radius R.

Supplementary References

1. Masias, A., Felten, N., Garcia-Mendez, R., Wolfenstine, J., and Sakamoto, J. (2019). Elastic, plastic, and creep mechanical properties of lithium metal. J. Mater. Sci. *54*, 2585–2600. https://doi.org/10.1007/s10853-018-2971-3.
2. Fincher, C.D., Ojeda, D., Zhang, Y., Pharr, G.M., and Pharr, M. (2020). Mechanical properties of metallic lithium: from nano to bulk scales. Acta Mater. *186*, 215–222. https://doi.org/10.1016/j.actamat.2019.12.036.
3. Masias, A., Felten, N., and Sakamoto, J. (2021). Characterizing the mechanical behavior of lithium in compression. J. Mater. Res. *36*, 729–739. https://doi.org/10.1557/s43578-020-00028-x.
4. Kozeny, J. (1927). Über kapillare Leitung des Wassers im Boden. Sitzungsberichte der Akademie der Wissenschaften in Wien *136*, 271–306.
5. Carman, P.G. (1997). Fluid flow through granular beds. Chemical Engineering Research and Design *75*. https://doi.org/10.1016/s0263-8762(97)80003-2.
6. Scott, G.D., and Kilgour, D.M. (1969). The density of random close packing of spheres. J. Phys. D Appl. Phys. *2*, 311. https://doi.org/10.1088/0022-3727/2/6/311.
7. Torquato, S., Truskett, T.M., and Debenedetti, P.G. (2000). Is Random Close Packing of Spheres Well Defined? Phys. Rev. Lett. *84*, 2064–2067. https://doi.org/10.1103/PhysRevLett.84.2064.
8. Roach, A.M., Zhu, W., Vema, S., McMeeking, R.M., Grey, C.P., Deshpande, V.S., and Fleck, N.A. (2025). Void growth in the lithium anode of a solid state battery. European Journal of Mechanics, A/Solids *113*. https://doi.org/10.1016/j.euromechsol.2025.105710.
9. Stallard, J.C., Vema, S., Grey, C.P., Deshpande, V.S., and Fleck, N.A. (2023). The strength of a constrained lithium layer. Acta Mater. *260*, 119313. https://doi.org/10.1016/j.actamat.2023.119313.